

# A Self-Assembled Binary Protein Model Explains High-Performance Salivary Lubrication from Macro to Nanoscale

Feng Xu, Evangelos Liamas, Michael Bryant, Abimbola Feyisara Adedeji, Efren Andablo-Reyes, Matteo Castronovo, Rammile Ettelaie, Thibaut V. J. Charpentier, and Anwesha Sarkar\*

Salivary pellicle, a spontaneously formed, intricate architecture in the human oral cavity, is a high-performance bio-lubricant that coats and protects biological surfaces with varying elastic modulus against frictional damage. Although salivary lubrication underpins the fundamentals of human feeding and speech, the peculiar molecular mechanism behind such lubrication properties remains elusive. For the first time, this work demonstrates a binary model comprised of salivary proteins, mucin, and lactoferrin (LF), forming an electrostatically driven, multilayered self-assembly that exhibits a lubrication behavior closely resembling that of human saliva, from macro to nanoscale. The multiscale tribological analysis with applied forces ranging from 1 N to 1 nN, supported by real-time self-assembly monitoring on hydrophilic and hydrophobic substrates differentially resolves the distinct roles played by the salivary proteins of this proposed lubricating model. Evidences reveal that hydrated mucin controls the macromolecular viscous lubrication entrapping water molecules in the mucinous network and LF acts as a “molecular glue” between mucin–mucin and mucin–surface, latter aiding boundary lubrication. This study puts forward an unprecedented molecular model that explains the synergistic lubrication by salivary components. These results can aid into the design routes for synthesizing highly efficacious nature-inspired aqueous lubricants for future biomedical applications and nutritional technologies.

and the minor components are salivary proteins and ions. Water is generally regarded as the “lubricant of life”<sup>[1]</sup> for all living organisms.<sup>[2,3]</sup> However, from an engineering perspective, water is an established poor lubricant owing to its limited adhesion to biological surfaces, poor load-bearing capacity, low pressure–viscosity coefficient, and thus behaves as a fluid under high confinement unlike nonpolar lubricants.<sup>[2]</sup> Hence, biological macromolecules in physiology are often cited as the protagonist in trapping water molecules within their complex network, rendering the ability to sustain high loads while presenting a fluid-like weeping response to shear under sliding contacts,<sup>[4]</sup> consequently providing ultra-low friction coefficients ( $\mu \approx 0.001$ ). In oral lubrication, these macromolecules are highly glycosylated multimeric salivary mucins that is the main protein component of salivary proteins besides  $\alpha$ -amylase, former constituting less than 1% of saliva.<sup>[5–7]</sup>

Saliva is unique as compared to all other bodily lubricants, as it bathes the hardest (enamel) to one of the softest tissues in the mouth.<sup>[8]</sup> However, a detailed

molecular-level understanding of such lubrication mechanism has remained elusive. Mucin, and more recently small molecular salivary proteins have been separately mooted as biological lubricants responsible for reducing friction in saliva. However, none of these by themselves have managed to replicate the remarkable aqueous lubrication in boundary and fluid

## 1. Introduction

Salivary pellicle, the absorbed layer of saliva within the oral cavity, is an excellent aqueous lubricant that maintains low-friction movement in the mouth that is of first-order importance to human life for feeding and speech. Interestingly, saliva consists of 99% water

F. Xu, Dr. E. Liamas, Dr. A. F. Adedeji, Dr. E. Andablo-Reyes, Dr. M. Castronovo, Dr. R. Ettelaie, Dr. A. Sarkar  
Food Colloids and Bioprocessing Group  
School of Food Science and Nutrition  
University of Leeds  
Leeds LS2 9JT, UK  
E-mail: A.Sarkar@leeds.ac.uk

 The ORCID identification number(s) for the author(s) of this article can be found under <https://doi.org/10.1002/admi.201901549>.

© 2019 The Authors. Published by WILEY-VCH Verlag GmbH & Co. KGaA, Weinheim. This is an open access article under the terms of the Creative Commons Attribution License, which permits use, distribution and reproduction in any medium, provided the original work is properly cited.

Dr. M. Bryant  
Institute of Functional Surfaces  
School of Mechanical Engineering  
University of Leeds  
Leeds LS2 9JT, UK

Dr. A. F. Adedeji, Dr. M. Castronovo  
Regional Referral Centre for Rare Diseases  
Azienda Sanitaria Universitaria Integrata di Udine  
33100 Udine, Italy

Dr. T. V. J. Charpentier  
School of Chemical and Processing Engineering  
University of Leeds  
Leeds LS2 9JT, UK

DOI: 10.1002/admi.201901549

film regimes as well as load-bearing abilities of adsorbed real human saliva in direct in vitro experiments.<sup>[9–13]</sup> Fundamental understanding of the salivary pellicle and the underpinning mechanisms of lubrication will enable the design and optimization of synthetic materials that emulate such functional architectures found in nature. This will have profound impact on the design of therapies for applications, such as polymedication-, cancer-, auto-immune disorders- or ageing-induced dry mouth conditions and associated infections,<sup>[14,15]</sup> mucosal drug delivery,<sup>[16]</sup> salivary dysfunction-induced speech disorders,<sup>[17]</sup> pleasurable nonobesogenic foods to easy-to-swallow foods,<sup>[18]</sup> and improved aqueous lubrication-based medical devices.<sup>[19,20]</sup> Without a doubt, a better understanding of the origins of friction in the oral environment is thus indispensable. Recognizing the growing evidence that molecular synergies in nature contribute to bio-lubrication at the tissue–fluid interface,<sup>[12,19–25]</sup> we hypothesize that the structural mechanism behind frictional characteristics of saliva to be a synergistic macromolecular self-assembly between its negatively and positively charged species.

This study sheds light on the molecular mechanism of salivary pellicle lubrication by involving multilayer fabrication using salivary proteins and multiscale lubrication experiments. Specifically, we have uncovered that an electrostatically driven multilayer architecture of binary salivary proteins, i.e., negatively charged

salivary mucin (bovine submaxillary mucin (BSM), 2.6 MDa) and positively charged salivary protein, lactoferrin (LF, 80 kDa), is key to facilitate the lubrication of soft sliding interfaces. Despite the simplicity of such a binary protein model compared to the complexity of multiple proteins in real saliva, the tribological properties of this architecture closely resemble those of real human saliva. Furthermore, we isolated the specific role of each protein component, and found that LF in saliva acts as a “molecular glue” in the mucin network that synergistically promotes mucin–mucin assembly to trap water molecules. Such a network facilitates macromolecule-mediated viscous lubrication, while the LF also glues salivary mucin strongly to the oral surfaces, thus enabling effective boundary lubrication. These unprecedented results present an optimal approach to study multiscale aqueous lubrication, and will open the doors to fabrication of nature-mimetic aqueous lubricants for a range of biological applications.

## 2. Results

To elucidate frictional dissipation and load-bearing behaviors of multilayered BSM/LF pellicle as compared to fresh human saliva, we involved several complementary, state-of-the-art tribological tools that span across length scales, i.e., a ball-on-disk

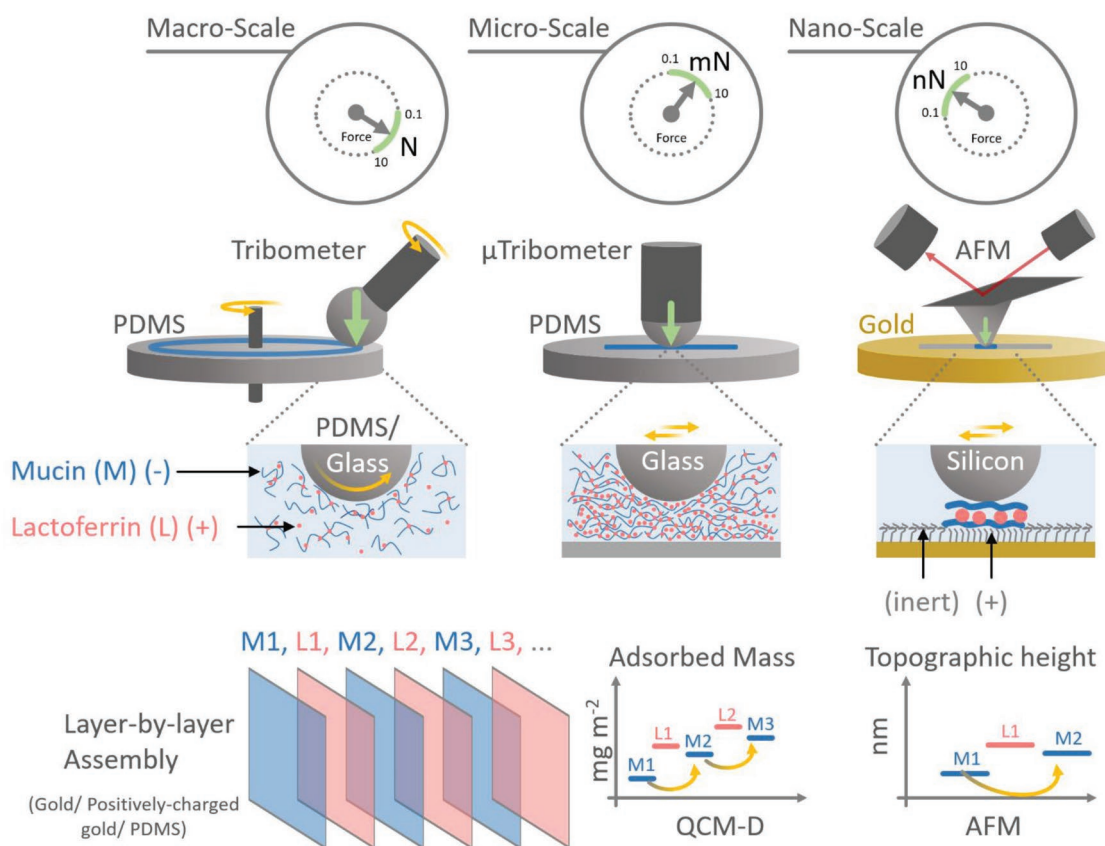


**Figure 1.** Methodology. Multiscale tribological and dynamic film-forming properties. a) From left to right (upper): Schematic diagrams of the tribological experiments of mucin (M)- LF (L) across length scales using a) ball-on-disk set up at macroscale (load, N), b) pin-on-plate set up at microscale (load, mN), and c) nanografting-assisted AFM at nanoscale (load, nN). d) From left to right (lower): Quantification of dynamic multilayered film formation (hydrated mass) on hydrophilic/hydrophobic substrates using QCM-D by recording frequency and dissipation shift upon protein adsorption followed by measuring topographic height using AFM at nanoscale.

set-up at the macroscale (Figure 1a), pin-on-plate set-up at the microscale (Figure 1b), and differential chemical force microscopy at the nanoscale (Figure 1c). The dynamic film formation of the multilayered architecture was quantified using a quartz crystal microbalance with dissipation monitoring (QCM-D) on substrates with varying surface chemistries (see detailed Experimental Section and the diagram in Figure 1d) supported by cryogenic scanning electron microscopy (cryo-SEM) of the films and contact angle measurement after deposition of the films onto hydrophobic surface. In addition, self-consistent field theory (SCF) calculations were applied to investigate the interactions between LF and BSM occurring between the two proteins at hydrophobic surfaces. Considering the physiological concentration of LF in real human saliva,<sup>[26]</sup> we explored our binary system at an orally relevant BSM/LF mass ratio and ionic conditions, which confirmed the binary proteins to retain opposite surface charges within the experimental window of stoichiometric and ionic parameters (see Figure S1a,b in the Supporting Information for zeta potential measurements).

### 2.1. Macroscale Lubrication—Entrainment Speed-Dependent Friction Coefficients

Using soft polydimethylsiloxane (PDMS) tribo-contact surfaces (see schematic in Figure 1a), the coefficients of friction,

$\mu$ , was measured as a function of entrainment speed for the two salivary proteins, their mixtures, the buffer, and of real human saliva. Figure 2a,b shows that for speeds in the range 0.001–0.01 m s<sup>-1</sup>, buffer corresponds to an upper bound for  $\mu$ , saliva to a lower bound (excellent lubricant), and model systems comprised of BSM and/or LF to intermediates  $\mu$  values, with only one binary BSM/LF system leading to saliva-compatible performance.

In particular, buffer provided high  $\mu$  values  $\geq 1.0$  in the plateau boundary regime ( $\bar{U} \leq 0.05$  m s<sup>-1</sup>), irrespective of the ion concentration (black crosses in Figure 2a,b). This is due to lack of its ability to adsorb to the PDMS substrate to form a load-bearing film as well as the adhesive nature of the bare hydrophobic PDMS–PDMS surfaces. The boundary lubrication of human saliva adsorbed to the PDMS tribo-pairs resulted in a  $\mu$  value (0.15) that is an order of magnitude lower than that of buffer (blue dots in Figure 2a,b). The large reduction in  $\mu$  for human saliva-lubricated surfaces is in agreement with the widely accepted assumption that the saliva firmly adsorbs onto ex vivo tribo-contact surfaces, forming a complex salivary conditioning film being similar to the salivary pellicle that builds in vivo onto dental enamel or mucosal surfaces.<sup>[27]</sup> This lubricating salivary layer further allowed fluid film entrainment contributing to subsequent reduction in  $\mu$  at higher speeds (0.01–0.5 m s<sup>-1</sup>), suggesting mixed dissipation regimes.

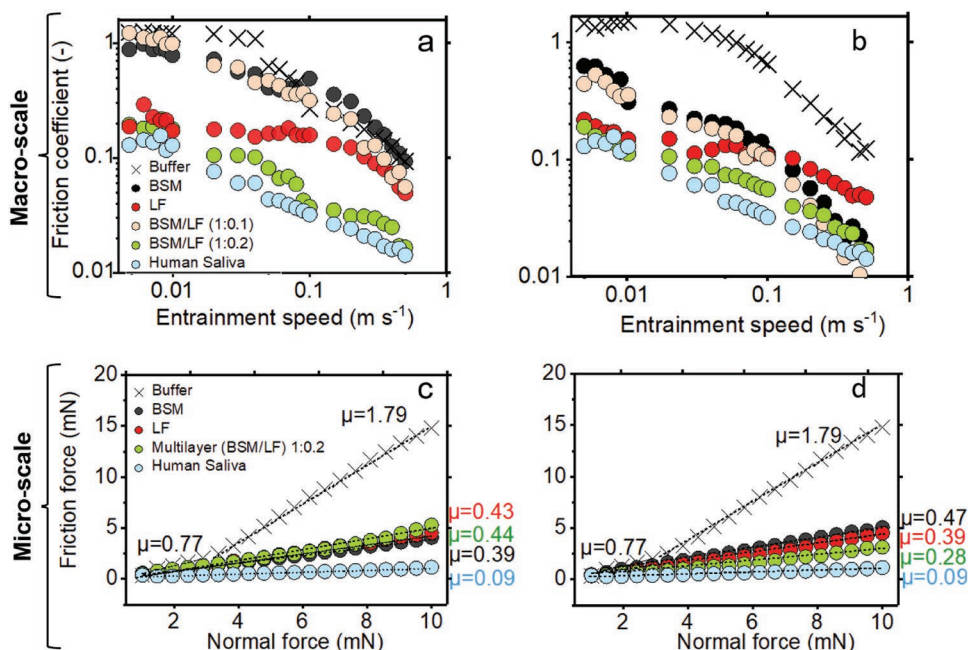


**Figure 2.** Friction force measurements of salivary proteins and human saliva from macro to microscales. Friction coefficients at macroscale were measured using ball-on-disk MTM tribometer (PDMS–PDMS soft contact surfaces) as a function of entrainment speeds at 2 N load and slide-roll ratio (SRR) of 50%. The influence of ionic concentrations a) 1 × 10<sup>-3</sup> M NaCl and b) 10 × 10<sup>-3</sup> M NaCl on lubrication properties of salivary proteins at macroscale was investigated. The ratio in BSM/LF systems indicates mass ratio, where BSM = 1 mg mL<sup>-1</sup>. Human saliva was collected from a healthy young female in the morning, subject was refrained from eating and drinking for at least 2 h before saliva collection (Ethics number: MEEC 16-046, University of Leeds, UK) and was diluted with 10 × 10<sup>-3</sup> M HEPES at the ratio of 1:1 w/w, centrifuged, and the supernatant was used for the tribology measurements. Friction forces ( $F_f$ ) at microscale were measured using pin-on-plate microtribometer (glass–PDMS contact surfaces) as a function of normal forces (1–10 mN). The applied normal load increased with distance in all experimental conditions. All the surfaces were prepared after an hour of adsorption by the salivary proteins or human saliva onto the PDMS surface and rinsing with their initial buffer solutions (10 × 10<sup>-3</sup> M HEPES) at c) 1 × 10<sup>-3</sup> M NaCl and d) 10 × 10<sup>-3</sup> M NaCl. Multilayers of BSM and LF were prepared by sequential adsorption of 2.5 bilayers of BSM/LF with both innermost and outermost layer of BSM. Friction coefficient ( $\mu$ ) was derived from slope of the best linear fits to the observed values of friction force versus normal force ( $R^2 > 0.98$ ).

BSM alone in a  $1 \times 10^{-3}$  M NaCl solution resulted in poor lubrication performance (black dots in Figure 2a), with the associated  $\mu$  values being close to those of buffer regardless of the entrainment speeds (see statistical analysis in Table S1, Supporting Information), suggesting macromolecular BSM was mostly squeezed out of the contact zone in the boundary regime. Another suggested reason for such high  $\mu$  values might be adhesive bridging interactions between BSM–BSM that arise when mucins are subjected to tribological stress between two hydrophobic surfaces, as reported in previous studies.<sup>[12,28]</sup> Increasing the ionic strength to  $10 \times 10^{-3}$  M NaCl (Figure 2b) significantly reduced the interfacial friction for BSM (see Table S2 in the Supporting Information for statistics), which might be attributed to partial adsorption of BSM onto the PDMS surface due to the charge screening effects (see Figure S1b in the Supporting Information for zeta potential measurements). Notably, the  $\mu$  values of BSM were close to those of human saliva only at  $10 \times 10^{-3}$  M NaCl and at entrainment speeds  $\geq 0.2$  m s<sup>-1</sup> (Figure 2b), suggesting a possible contribution of BSM in providing a macroscopic elasto-viscous lubrication.

Although an unprecedented behavior, LF alone resulted in excellent boundary lubrication, with  $\mu$  values closely resembling those of human saliva at low entrainment speeds (boundary regime), regardless of the ionic strength (Figure 2a,b). The lubrication profile of LF significantly deviated from human saliva in mixed lubrication regime at entrainment speeds  $\geq 0.05$  m s<sup>-1</sup> (Figure 2a,b). The results suggest that despite LF being superior to BSM in terms of boundary lubrication where physical adsorption dominates, the speed-dependent lubrication performance of LF and BSM inversely ranked. In other words, LF alone, unlike BSM, was unable to provide sufficient hydrodynamic lift to keep the  $\mu$  low on the way to the hydrodynamic lubrication regime.

In contrast to the separate lubrication performance of BSM and LF, the lubrication of the binary BSM/LF system at 1:0.2 mass ratio (green dots in Figure 2a,b) showed a dramatic reduction in  $\mu$  both in the boundary and the mixed regimes similar to human saliva. Especially at  $10 \times 10^{-3}$  M NaCl (Figure 2b), such a binary system was better entrained and accelerated the onset of mixed lubrication regime as compared to BSM and LF alone. Mixing BSM and LF at 1:0.1 mass ratio instead, displayed a behavior very similar to the one of BSM alone (beige dots in Figure 2a,b), therefore suggesting that the lubrication properties of the binary BSM/LF system are associated with specific structural determinants and optimal stoichiometric ratio between BSM and LF.

Experiments were also performed using hydrophilic borosilicate glass-on-PDMS substrate (see Figure S2, Supporting Information) using the optimal BSM/LF binary system (1:0.2) to serve as a control for microscale tribology experiments (discussed in the next section). As one can anticipate, the buffer and BSM showed an order of magnitude lower  $\mu$  values in the boundary regime in this hydrophilic–hydrophobic contact (see Figure S2, Supporting Information) as compared to the hydrophobic PDMS–PDMS counterparts (Figure 2b) owing to enhanced entrainment of buffer or BSM films in the former. Such reduction in  $\mu$  values by changing the material chemistry of substrates is in close agreement with the previous results on Newtonian fluids using hydrophilic–hydrophobic contact

surfaces.<sup>[29]</sup> Of more relevance is the fact that it was only the binary BSM/LF system at 1:0.2 mass ratio that matched the boundary lubrication behavior of real human saliva at the speeds used in the microscale experiments (discussed below).

## 2.2. Microscale Lubrication—Load-Bearing Ability of Salivary Films

Using a microtribometer (see schematic in Figure 1b), we investigated lubrication phenomena of the salivary film and the binary protein models via mechanical sliding in dynamic oral environment with lower normal loads (mN) and sliding speeds. According to the modified Amonton's law,<sup>[30]</sup> in the low contact pressure, plotting the sliding friction force,  $F$ , against the applied loads,  $F_N$ , gives a direct measure of  $\mu$  by using Equation (1), where  $C$  is the interfacial adhesive force

$$F = \mu F_N + C \quad (1)$$

A two-phase  $F - F_N$  curve was observed. Between 0.1 and 3 mN,  $\mu$  (the slope of the linear regression fit) of 0.77 was observed. With the increase of  $F_N$  from 3 to 10 mN, a sudden increase of  $\mu$  between the buffer-bathed surfaces was observed, due to adhesion between the sliding surfaces (Figure 2c,d, see the normal force profile vs sliding amplitudes in Figure S3a,b, Supporting Information). Although, water is a major component of most aqueous bio-lubrication in nature, it is unable to produce load-bearing lubricating films at high pressures and low sliding speeds. Human saliva, on the other hand, demonstrated highest lubrication performance with  $\mu = 0.09$ ; being consistent across the loading range (Figure 2c). Adsorption of BSM at microscale prevented the sudden increase of  $\mu$  within the range of contact pressures used. This can be explained by the adsorption of amphiphilic BSM to a certain degree onto the hydrophobic PDMS surfaces (Figure 2c,d) and gradual removal of the hydrophobic adhesive forces between tribo-surfaces via a macromolecule-mediated viscous lubrication mechanism. Compared to the macroscale lubrication behaviors presented in Figure 2a,b, such an analysis reveals that BSM outperforms the buffer as a microscale lubricant (Figure 2c,d). In addition, the measured  $\mu$  value of BSM ( $\mu = 0.39$  and  $0.47$  at  $1 \times 10^{-3}$  and  $10 \times 10^{-3}$  M NaCl, respectively) is near the values reported by other groups.<sup>[31–33]</sup> The microscale analysis also reveals that LF (Figure 2c,d) did not reduce  $\mu$  as occurred at the macroscale (Figure 2a) despite it adsorbing to the tribological surface. Nevertheless, at the microscale, the multilayered BSM/LF (1:0.2)<sub>2.5</sub> system (see the Experimental Section for preparation) at  $10 \times 10^{-3}$  M NaCl still continues to provide the best lubrication performance among all the other samples, tending toward human salivary  $\mu$  values (Figure 2d). The discrepancy in  $\mu$  values between the multilayered system BSM/LF (1:0.2) and the human saliva might be attributed to the lubrication properties of other lubricating components present in the human saliva, such as statherin<sup>[10]</sup> that is unavailable in the binary self-assembled model, proposed in this study.

In order to elucidate the load-bearing properties of the multilayered BSM/LF (1:0.2)<sub>2.5</sub> system versus real human saliva, Figure 3 shows the effective friction coefficient ( $\mu_{\text{eff}}$ ) as a function of the sliding cycle (for over 50 cycles) and applied

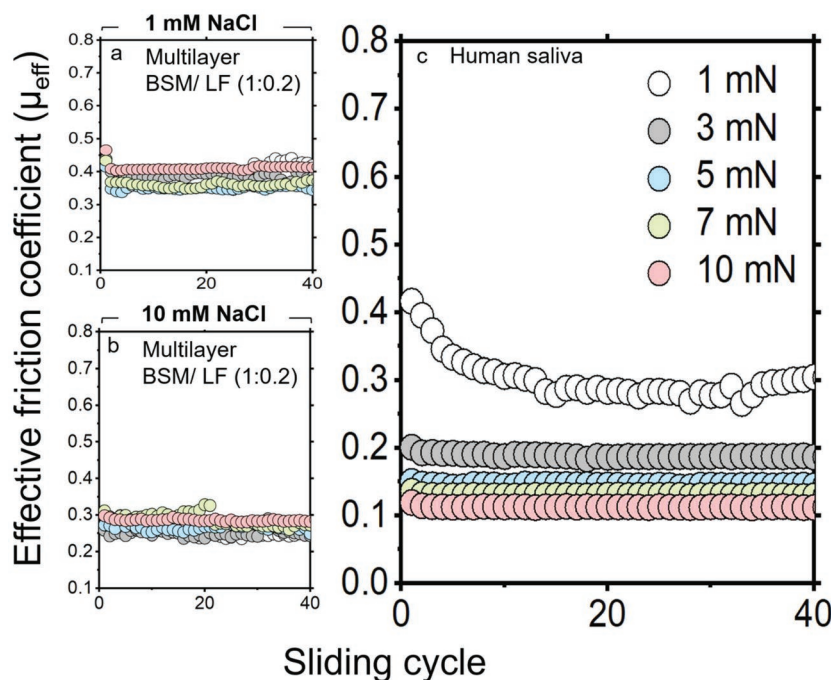


**Figure 3.** Effective friction coefficient of salivary proteins and human saliva as a function of sliding cycles. Effective friction coefficient ( $\mu_{\text{eff}}$ ) at microscale was measured using pin-on-plate nanotribometer (glass-PDMS contact surfaces) with an incremental increase of the normal load. To assess load-bearing characteristics of the salivary protein films, the friction coefficient was continuously measured over 50 cycles under each load. The representative friction coefficient under 1, 3, 5, 7, 10 mN was plotted as a function of sliding cycle for a) multilayer BSM/LF (1:0.2) with 2.5 bilayers at  $1 \times 10^{-3}$  M NaCl, b) BSM/LF (1:0.2) with 2.5 bilayers at  $10 \times 10^{-3}$  M NaCl, and c) human saliva. Human saliva was collected from a healthy and young female in the morning, subject was refrained from eating and drinking for at least 2 h before saliva collection (Ethics number: MEEC 16-046, University of Leeds, UK) and was diluted with  $10 \times 10^{-3}$  M HEPES at the ratio of 1:1 w/w, centrifuged, and the supernatant was used for tribology measurements.

load (1–10 mN) relative to the microscale tribology data shown in Figure 2c,d, for the multilayered BSM/LF (1:0.2)<sub>2.5</sub> system at  $1 \times 10^{-3}$  M NaCl (Figure 3a) and  $10 \times 10^{-3}$  M NaCl (Figure 3b), and human saliva (Figure 3c), which successfully formed boundary layers on the PDMS surface. Figure 3 shows that the back-and-forth sliding at normal loads  $>1$  mN did not result in any significant increase in  $\mu_{\text{eff}}$  for these systems (see also Figure S4a–d in the Supporting Information for LF or BSM monolayers). It is noteworthy that  $\mu_{\text{eff}}$  for the multilayered BSM/LF (1:0.2)<sub>2.5</sub> system at  $1 \times 10^{-3}$  M NaCl (Figure 3a) was higher than that of human saliva (Figure 3c), while at  $10 \times 10^{-3}$  M NaCl (Figure 3b) the lubrication behavior closely resembles that of human saliva (Figure 3c). As can be expected, BSM/LF systems involve electrostatic interaction of BSM with LF. The increased ion concentration reduces the Debye screening length (calculated to be 9.5 and 3 nm in  $1 \times 10^{-3}$  and  $10 \times 10^{-3}$  M NaCl solutions, respectively<sup>[34]</sup>) resulting in less repulsion within the protein layers at higher ion concentration (see Figure S1b in the Supporting Information for zeta-potential).

For relating the  $\mu$  values in macroscale and microscale tribology experiments with glass-on-PDMS substrates, we calculated the relative  $\mu$  values of the samples to that of the buffer ( $\mu_{\text{R}}$ ) (see also Figure S5, Supporting Information). It is interesting to note that irrespective of macro and microscales,  $\mu_{\text{R}}$

values showed similar pattern with BSM/LF system showing the lubricating behavior tending toward human saliva as compared to the sole salivary protein components. The difference in absolute values of the  $\mu_{\text{R}}$  might be attributed to the adhesion energy in microscale and sliding conditions used at microscale as compared to sliding-to-rolling conditions used in the macroscale experiments. Also, the contact pressure difference between the two systems (see the Experimental Section) might explain such differences in absolute  $\mu_{\text{R}}$  values.

In summary, tribology measurements at the macro and microscale indicate that in the BSM/LF binary system at 1:0.2 mass ratio, the two proteins synergistically form an optimum macromolecular architecture, in which LF interacts with the surface to form a robust boundary layer, and hydrated BSM layers are responsible for entrapment of water molecules that promote viscous lubrication in the mixed regimes. In such an architecture, the binary protein system emulates salivary lubrication particularly in higher ion concentration. This electrostatic contribution might be attributed to both intrinsic charge compensation between LF and BSM as well as extrinsic charge compensation contributed by the charge screening ions. To understand the structural mechanism underpinning the uncovered lubrication phenomena, we investigated the properties of multilayer assemblies involving BSM and LF with QCM-D (see schematic in Figure 1d) and atomic force

nanolithography and microscopy (see schematic in Figure 1c) as it follows.

### 2.3. Fabrication of Multilayered Assembly of Binary Proteins

The QCM-D results indicated an almost instantaneous ( $0.14 \text{ mg m}^{-2} \text{ s}^{-1}$ ) and substantial adsorption by human saliva, yielding hydrated mass of  $\approx 30 \text{ mg m}^{-2}$  (see Figure S6, Table S3 (Supporting Information) is provided for the hydrated mass calculation parameters), which is in the line with previous studies.<sup>[10,34]</sup> Figure 4 displays the adsorption of the subsequently deposited multilayer build-up by the binary proteins, and schematic representations for protein adsorption over the different surfaces (see frequency/dissipation shifts in Figure S7 in the Supporting Information, thickness of the architecture in Figure S8 in the Supporting Information, and cryo-SEM image of multilayered architecture of BSM/LF in Figure S9 in the Supporting Information). First, the degree of adsorption ( $\approx 25\text{--}45 \text{ mg m}^{-2}$ ) (Figure 4a,e,i) and kinetics ( $0.1\text{--}0.15 \text{ mg m}^{-2} \text{ s}^{-1}$ , Figure S7, Supporting Information) by the multilayered architecture uniquely resembled those of real human saliva (see Figure S6, Supporting Information), which justifies the

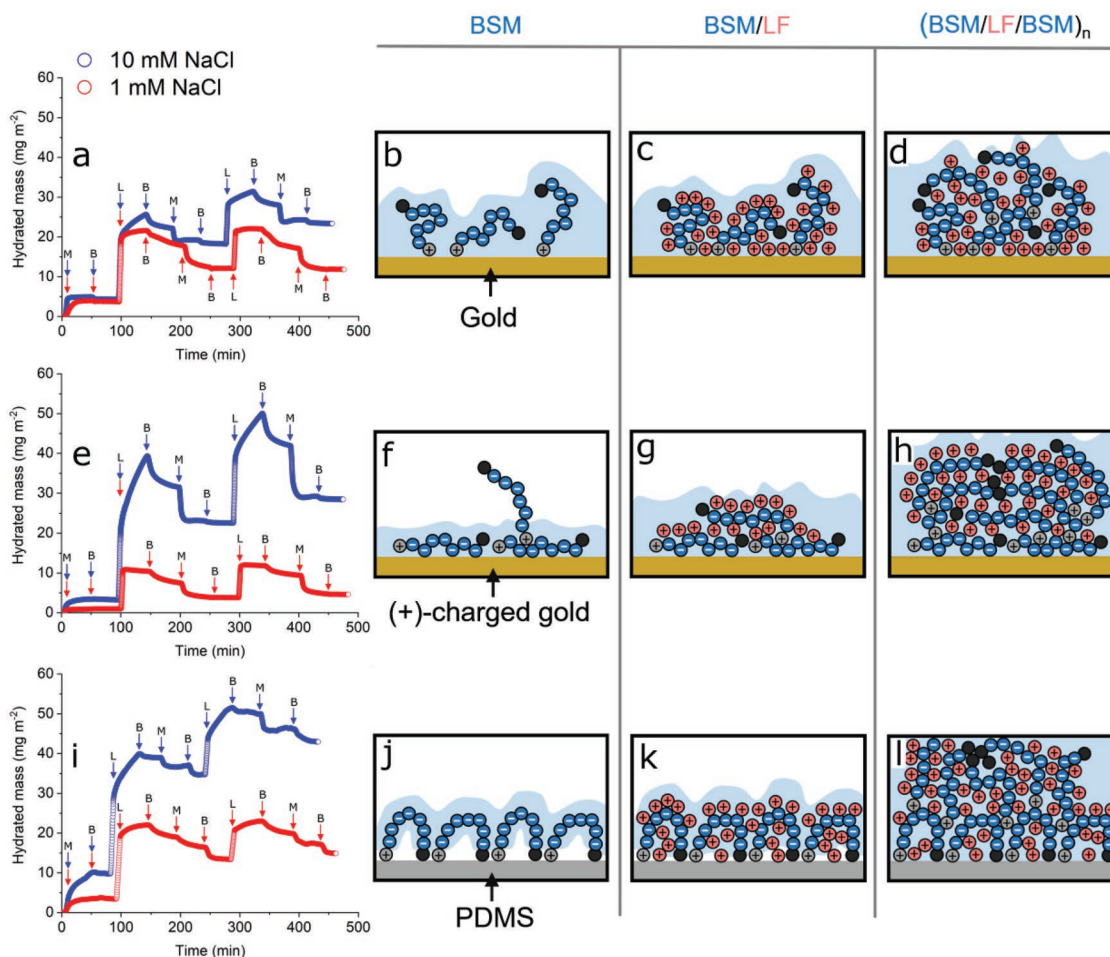


**Figure 4.** Real-time adsorption of salivary proteins in the QCM-D as a function of ionic concentration and substrates. Monitoring real-time individual protein layer deposition using QCM-D: Evolution of the hydrated mass for layer-by-layer build-up derived using Voigt viscoelastic model applied to the 3rd–11th overtones (raw data of frequency and dissipation shifts of 5th overtone are available in Figure S7, Supporting Information). Influence of ionic concentration on multilayer build-up of BSM and LF was investigated on a–d) hydrophilic gold sensor, e–h) positively charged gold sensor, and i–l) hydrophobic PDMS-coated sensor at BSM/LF (1:0.2) mass ratio and their corresponding schematic representations with blue background representing water attached to the proteins. For layer-by-layer self-assembly, BSM (M) and LF (L) labels indicate the beginning of the BSM or LF adsorption step, respectively. The BSM and LF were left to adsorb for 45 min, followed by 45 min of rinsing with  $10 \times 10^{-3}$  M HEPES buffer (B) in the presence  $1 \times 10^{-3}$  or  $10 \times 10^{-3}$  M NaCl. In all the conditions, the multilayer of BSM and LF built up with a nonmonotonic cyclic behavior observed using QCM-D. Each trilayer (BSM/LF/BSM) resulted in a net positive increment of adsorbed mass on different underlying surfaces and at different ionic concentrations.

findings of similar  $\mu$  values of BSM/LF and human saliva in the adsorption-driven boundary regime in macro to microscales (Figure 2a–d; Figure S2, Supporting Information).

In Figure 4a,e,i, all curves shared a similar qualitative behavior in that a two-stage film formation is evidenced but with difference in the degree of adsorbed hydrated mass depending on the substrate. Initially, just focusing on the mass adsorption behavior, the two-step addition of BSM followed by LF to form the first bilayer led to a step-wise increase in the hydrated mass, with LF adsorption being two-to-four times higher than that of BSM due to intrinsic charge compensation. Rinsing with the buffer removed the loosely bound hydrated LF molecules (about  $2\text{--}8 \text{ mg m}^{-2}$ ). Subsequently, a further decrease of the hydrated mass occurred in response to addition of a second BSM layer over the initial bilayer. This mass loss indicates the presence of some loosely bound LF to form a heteroprotein complex<sup>[35]</sup> with the BSM in bulk phase. The other

possibility is that some of the loosely bound LF molecules were removed from the film and substituted by BSM that had higher affinity toward the adsorbed LF layer, rearranging the LF/BSM layer at the surface. Close inspection of such an alternating film growth as a function of protein layers shown in Figure 4a,e,i reveals that each cycle has modified to the adsorbed layers with a net positive increment of the total mass of BSM from  $5\text{--}10$  to  $20\text{--}35 \text{ mg m}^{-2}$ . With further addition of LF/BSM layer, the hydrated mass increases by another  $25\text{--}30\%$ , highlighting the importance of layer formation contributing to the total hydrated mass that resembles that of real human saliva in corresponding substrate (see Figure S6, Supporting Information).

It is worth mentioning that LF continues to adsorb and does not reach an equilibrium even after several hours both on top of a BSM monolayer (Figure S10a–d, Supporting Information) as well as when added directly on a gold substrate (Figure S10e–h, Supporting Information). This can be

anticipated as the molecular structure of LF at pH 6.8 resembles a dipole,<sup>[36]</sup> with a negative patch on one end and a large positive patch on the other end at neutral pH. As a result, LF can adsorb onto other LF molecules with electrostatic interaction between negative patches of one LF and positive patches in another LF. Thus, rinsing with buffer for 45 min results in 5–15% loss of hydrated LF molecules depending upon the substrate. However, addition of BSM to LF is preferred over LF to LF owing to more favorable electrostatic attraction with the former.<sup>[37]</sup>

The nonmonotonic cyclic growth behavior observed in this study has been previously reported in biological polyelectrolytes such as proteins,<sup>[25,38,39]</sup> where a perfect sandwich-like layer-by-layer growth pattern was not evident. In fact, proteins inter-layer diffusions eventually leading to a more blended “fuzzy” multilayer assembly lacking controlled order in semi-dilute conditions are more common.<sup>[40–42]</sup> Noteworthy, that the behavior of the nonmonotonic cyclic growth in this study was also reproduced when the first layer to adsorb on the selected substrates was LF (Figure S11, Supporting Information), resulting in similar levels of adsorbed masses when compared to Figure 4a,i. Besides partial dissolution of the precursor layer, the loss of mass observed from QCM-D (i.e., measuring hydrated mass) in this study may partly result from weeping out of water molecules attached tenaciously to the LF/BSM layers,<sup>[43–46]</sup> which may provide the fluid film lubrication as observed previously (Figure 2a–d). This was further supported macroscopically by the multilayered (BSM/LF)<sub>2,5</sub> architecture built with 2.5 bilayers (i.e., BSM/LF/BSM/LF/BSM) that uniquely rendered substantial hydrophilicity to the otherwise hydrophobic PDMS sensors, resulting in one order of magnitude reduction in static water contact angle (from 102.7° to < 10°), comparable to that of real human saliva, and such hydrophilicity was restored even after 72 h (see Figure S12, Supporting Information).

### 2.3.1. Substrate Chemistry Dependence

Multilayer structure can be divided into three zones: I) a precursor zone, i.e., the zone at the liquid-substrate interface, II) a core zone, and III) an outer zone, where the layer in the zone I is directly influenced by the properties of the supporting substrate.<sup>[47]</sup> We studied the influence of substrate using untreated hydrophilic gold surface, amine-terminated positively charged gold surface (water contact angle < 10°), and hydrophobic PDMS surface (water contact angle is 102.7 ± 0.9°) to represent a wide span of physiologically relevant oral surfaces from surface chemistry viewpoint, i.e., normal oral mucosal surfaces to acute dry mouth patients’ oral surfaces (hydrophobic) having almost no salivary residues. Surface morphology of the first BSM layer as well as its influence to the subsequent layers additions is schematically illustrated in Figure 4b–d,f,h–j,l).

Interestingly, the substrates had a significant influence on the adsorption behavior of not only the first BSM layer but also the subsequently layers. The lowest value of adsorbed material for the first BSM layer occurred on the hydrophilic gold and the amine-terminated surfaces (Figure 4a,e), in line with other studies,<sup>[48,49]</sup> suggesting that hydrophilic interaction was least preferred by BSM at the surface. The weakly negatively charged gold surface most likely allowed the

single-end anchoring by the positively charged N-terminal of mucin, thus resulting in a random 3D spatial arrangement (schematic representation of the first layer shown in Figure 4b). The parameter,  $-\Delta D/\Delta f$  (where  $\Delta D$  and  $\Delta f$  are changes in dissipation and frequency, respectively) is commonly used to indicate the film properties; a higher  $-\Delta D/\Delta f$  is often associated with a more viscous/less elastic film and vice versa.<sup>[10,50,51]</sup> The lowest value of  $-\Delta D/\Delta f$  achieved by BSM film on the hydrophilic gold surface (Figure S13, Supporting Information) suggests that it was less viscous and had a relatively rigid structure resulting in least adsorbed mass (Figure 4a) in comparison to the other two substrates. Addition of LF makes it more compact (Figure S13, Supporting Information) even with the doubling of the hydrated mass (Figure 4c). The pattern repeats itself with further addition of layers with BSM contributing to the viscosity of the layer whereas LF compacts the BSM layers (Figure 4d).

The diagram in Figure 4e depicts adsorption of BSM onto the positively charged surface owing to the electrostatic interactions between the positively charged surface and negatively charged central domains of BSM chains. The electrostatic interactions enable most of the BSM molecules to lay down flat on the surface (see diagram in Figure 4f) thus resulting in lower hydrated mass (Figure 4h). Subsequent introduction of LF results in adsorption onto the formed BSM layer due to attractive electrostatic interactions between LF and BSM (Figure 1a,b, Supporting Information), which significantly increases the adsorbed mass after formation of the second bilayer (Figure 4g), and increases the rigidity of the heteroprotein layer (Figure S13, Supporting Information). Since LF has an overall positive net charge, it interacts electrostatically only with the BSM-coated surface rather than the amine-terminated positively charged surface gold surface as latter is covered by a layer of BSM (Figure 4g). The overall network has significantly higher hydrated mass as compared to the gold surface supported by electrostatic interactions between BSM and LF (Figure 4h). However, the heteroprotein complexation between LF and BSM in the bulk phase cannot be ignored, resulting in higher mass removal during buffer rinsing (Figure 4e) as compared to that of the untreated gold surface (Figure 4a).

For the hydrophobic PDMS surface, the first BSM layer adsorbs to the highest extent (Figure 4i) as compared to the gold and positively charged surfaces (Figure 4a,e), highlighting BSM favoring a hydrophobic interaction with the surface as compared to the hydrophilic surfaces (Figure 4a,e). Attachment of mucins to hydrophobized mica surfaces via the hydrophobic globular regions in mucins has been reported previously with other variants of mucins.<sup>[28]</sup> As described by Chang et al.,<sup>[52]</sup> glycoproteins tend to adopt a compact loop-like structure on hydrophobic surface, where the hydrophobic globular domains in the N- and C-terminal regions of mucins anchor on the surface (see diagram in Figure 4j). Such a mechanism involves the hydrated central domain of BSM protruding from the surface, thus leading to an overall higher hydrated mass, which corroborates the findings of viscous lubrication observed in Figure 2a–d with the PDMS tribopairs. The LF is known to have the ability to adsorb onto both hydrophilic gold and hydrophobic PDMS surfaces.<sup>[53]</sup> Hence, in parallel to electrostatically

interacting with the porous BSM matrix (see cryo-SEM image of BSM and LF in Figure S9, Supporting Information), the globular LF molecule could penetrate (owing to a hydrodynamic diameter of 4–8 nm<sup>[35]</sup>) through the pores within the 3D BSM architecture and adsorb to the unbound PDMS surfaces, resulting in the increase of the hydrated mass (Figure 4i,k,l) as well as supporting the boundary lubrication demonstrated in Figure 2a–d.

One should note that although gold and PDMS substrates show similar rigidity of the final bilayers (Figure S13, Supporting Information), the PDMS renders higher hydrated mass in BSMS/LF bilayers (45 mg m<sup>-2</sup>) as compared to that of gold (25 mg m<sup>-2</sup>). This might be attributed to the loop-like structure of BSM (Figure 4j) on PDMS that provides more surface for LF to bind onto the negatively charged central domain of BSM and does not allow LF to deplete as much during the buffer-rinsing step (< 2 mg m<sup>-2</sup> in first and ≈5 mg m<sup>-2</sup> in the second bilayer, respectively) (Figure 4i) as seen in the amine-terminated gold surface (removal in buffer rinsing step < 10 mg m<sup>-2</sup> in first and ≈15 mg m<sup>-2</sup> in the second bilayer, respectively) (Figure 4e).

Interestingly, both the first BSM layer and the assembly of the multilayer architecture were substantially substrate-dependent (Figure 4d,h,l). Particularly the one with PDMS shows the most promising behavior resulting in highest adsorption by the multilayered architecture (45 mg m<sup>-2</sup>) corroborating the lubrication results of Figure 2a,b using PDMS–PDMS set up. Also it is worth noting that the first protein layer (either LF or BSM) plays an important role in the multilayer architecture. Just by changing the first layer to LF instead of BSM (Figure S11, Supporting Information) reverses the adsorption behavior on PDMS and gold, with the latter having much more adsorbed mass as compared to the one having BSM as the first layer (Figure 4a). This is not surprising as the presence of LF as the first layer disables BSM to form the loop-like structure to bind subsequently more LF as seen in Figure 4l for the PDMS counterparts.

### 2.3.2. Ionic Concentration Dependence

Consistent with the tribology results shown in Figures 2b,d and 3b, the adsorption of these weak polyelectrolytes, i.e., BSM and LF is highly sensitive to ionic concentration, as shown in Figure 4a,e,i. BSM adsorption is higher in a 10 × 10<sup>-3</sup> M NaCl solution at first cycle, particularly in PDMS, and subsequent cycles irrespective of the substrates. The electrostatic screening of repulsion between like protein molecules, resulting from the addition of salt (10 × 10<sup>-3</sup> M), allows more BSM and LF to bind to the surface in comparison to lower ionic concentration (1 × 10<sup>-3</sup> M). Although it is worth noting that at the same time higher electrolyte concentrations also weaken the attractive interactions between oppositely charged LF and BSM molecules. This finding is in agreement with BSM showing negligible frequency shift without the presence of ions (see Figure S14a, Supporting Information), and findings of Lundin et al.<sup>[54]</sup> that BSM forms a more rigid film indicated by the lower  $-\Delta D/\Delta f$  on increased ion concentration (see Figure S14b, Supporting Information). Such screened intra and interelectrostatic

repulsion resulting in the higher adsorption has been also observed in real human saliva in ex vivo experiments.<sup>[55,56]</sup> Owing to the highly stable ionic hydration shells, water molecules could be added during real-time multilayer structure formation via extrinsic charge compensation, thus leading to an increase of the hydrated layer mass.<sup>[57]</sup> This phenomenon is often considered in ultrathin multilayered systems,<sup>[58]</sup> as well as known to influence boundary lubrication (Figures 2b,d and 3b).

### 2.4. SCF Theory

In order to understand in greater depth the synergistic interaction between LF and BSM as suggested by our observed tribology results (Figures 2–4), we used the well-known SCF theory<sup>[59,60]</sup> to calculate the equilibrium volume fraction profiles of the adsorbed LF and BSM proteins across the surface film, both on their own and when they are present simultaneously together in the (BSM/LF/BSM)<sub>n</sub>. It is noteworthy that LF was modeled using its complete 708 amino acid residues, grouped into five distinct sets, while for BSM, a simplified version consisting of 2060 residues was employed (see the Experimental Section for details). The calculations were all carried out at a salt volume fraction of 0.002, roughly corresponding to 10 × 10<sup>-3</sup> M NaCl, i.e., the ionic conditions, where most beneficial lubrication properties and adsorption behaviors were observed (Figures 2–4).

The LF segments tended to reside closer to the hydrophobic interfaces (see Figure S15a-i, Supporting Information) supporting the high adsorption behavior seen in QCM-data when using PDMS surfaces (Figure 4i–l). As can be anticipated, the density profiles calculated using SCF showed that BSM segments formed a clear loop (similar to the schematic in Figure 4j) with an interfacial coverage that was three orders of magnitude lower (in mole per unit area terms) at the surface as compared to those of the LF segments when present on their own (see Figure S15b-i, Supporting Information). In other words, BSM with its large hydrophilic segments tended to adsorb far less and was stretched further away from the surface, forming less dense layers and not contributing significantly to boundary lubrication (Figure 2a,b). Any contribution made by BSM is more likely due to bridging mechanisms as discussed elsewhere.<sup>[28]</sup> Likewise the interaction potentials derived from SCF calculation for LF and BSM, each on their own, as induced between two flat parallel planes also revealed major quantitative differences between LF and BSM (see Figure S15a-ii,b-ii, Supporting Information), highlighting LF to favor the hydrophobic surface.

Of more relevance here for the tribological behavior is the interaction between LF and BSM in a short gap distance (say of ≈20 nm) where we compared the behavior of LF and BSM on its own versus that with both proteins simultaneously present together in (BSM/LF/BSM)<sub>n</sub> multilayered architecture as shown in Figure 5. In case of LF, there is no significant difference in segment density profile when present on its own (Figure 5a-i) or in a multilayered system (Figure 5a-ii). However, in contrast the amount of BSM was increased dramatically in the gap by a factor of ≈3 when present in (BSM/LF/BSM)<sub>n</sub> multilayered architecture (Figure 5b-ii) as opposed to being present on its own (Figure 5b-i), supporting the lubrication synergy discussed

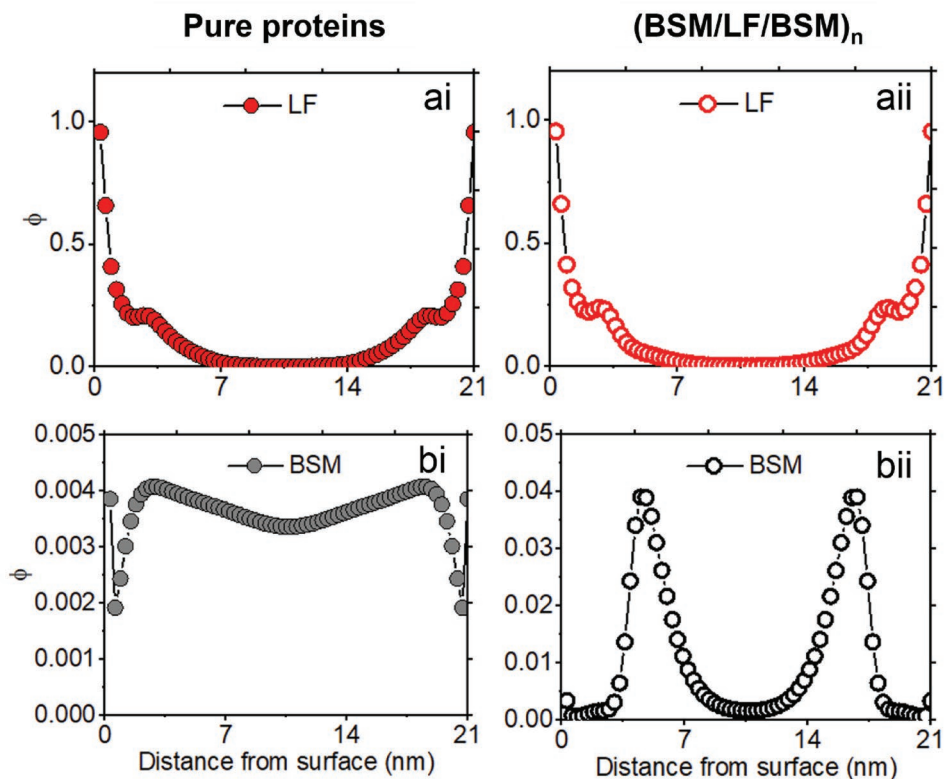


**Figure 5.** SCF theory calculations of total segment density profiles for the salivary proteins. Total segment density profiles are plotted as a function of distance in the gap between two flat parallel hydrophobic surfaces separated by a distance of 70 monomer units, i.e., 21 nm for a) LF on its own and b) BSM on its own (i) or when present in the multilayered system (LF/BSM/LF)<sub>n</sub>. Remaining protein bulk volume fraction is  $1 \times 10^{-7}$  in each case, as it is assumed that most of protein will be adsorbed, and ion volume fraction is 0.002 (equivalent to  $10 \times 10^{-3}$  M NaCl) at neutral pH.

before. In the absence of LF, BSM is not strongly enticed to adsorb on the surface. Not perhaps surprising when considering the highly charged hydrophilic residues (the middle overwhelmingly hydrophilic segment of this protein, modeled here as consisting of 2000 monomers), and the significant entropic losses involved when such large chains adsorb. However, in the presence of LF, the synergistic electrostatic interaction between these two oppositely charged proteins more than compensates for this loss of entropy, favoring BSM to be at the surface and corroborating our QCM-results reported here. In other words, LF will allow binding of more BSM by favorably interacting with it (see Figure S1b in the Supporting Information for zeta-potential values of cationic LF and anionic BSM) to compensate for any loss of configurational entropy by the latter during its adsorption. Furthermore, build-up of a negative surface charge, preventing further adsorption of BSM, is achieved at a lower amount of adsorbed BSM if the surface is not charged, than if it was positively charged due to the presence of an interfacial film of LF.

## 2.5. Nanoscale Lubrication

### 2.5.1. Nanolithography Approach

Finally, to provide direct evidence of the structural and tribological properties of the precursor zone of the BSM/LF multilayer,

we adopted a genuinely differential nanoscopy approach based on atomic force microscopy (AFM), which allowed for investigation of the BSM/LF multilayer at  $10 \times 10^{-3}$  M NaCl in response to applied forces in the nN range, as shown in Figure 1c, leading to results presented in Figure 6.

In our approach, we exploited an AFM tip-induced nanolithographic technique termed nanografting to form square patches of a few  $\mu\text{m}$  in size of monolayer of a positively charged alkylthiol within a preformed self-assembled monolayer (SAM) of an ethylene glycol-terminated (TOEG) alkylthiol supported by an ultra-flat gold surface (see Figure S16, Supporting Information). The key advantage of our approach is in that TOEG-SAM is known to resist protein adsorption in aqueous media, and therefore it provided with an invariable reference layer for quantifying differential thickness<sup>[61,62]</sup> and friction changes at nanoscale<sup>[63]</sup> over the nanografted patch in response to the salivary protein adsorption.

### 2.5.2. Differential Nanoscopy

While topographic height differences between surface features are typically accurately measured by AFM, changes in friction coefficient are much harder to determine by AFM with comparable calibration accuracy.<sup>[63]</sup> Indeed, AFM friction is generally defined as the difference between lateral force traces that are measured along opposite directions

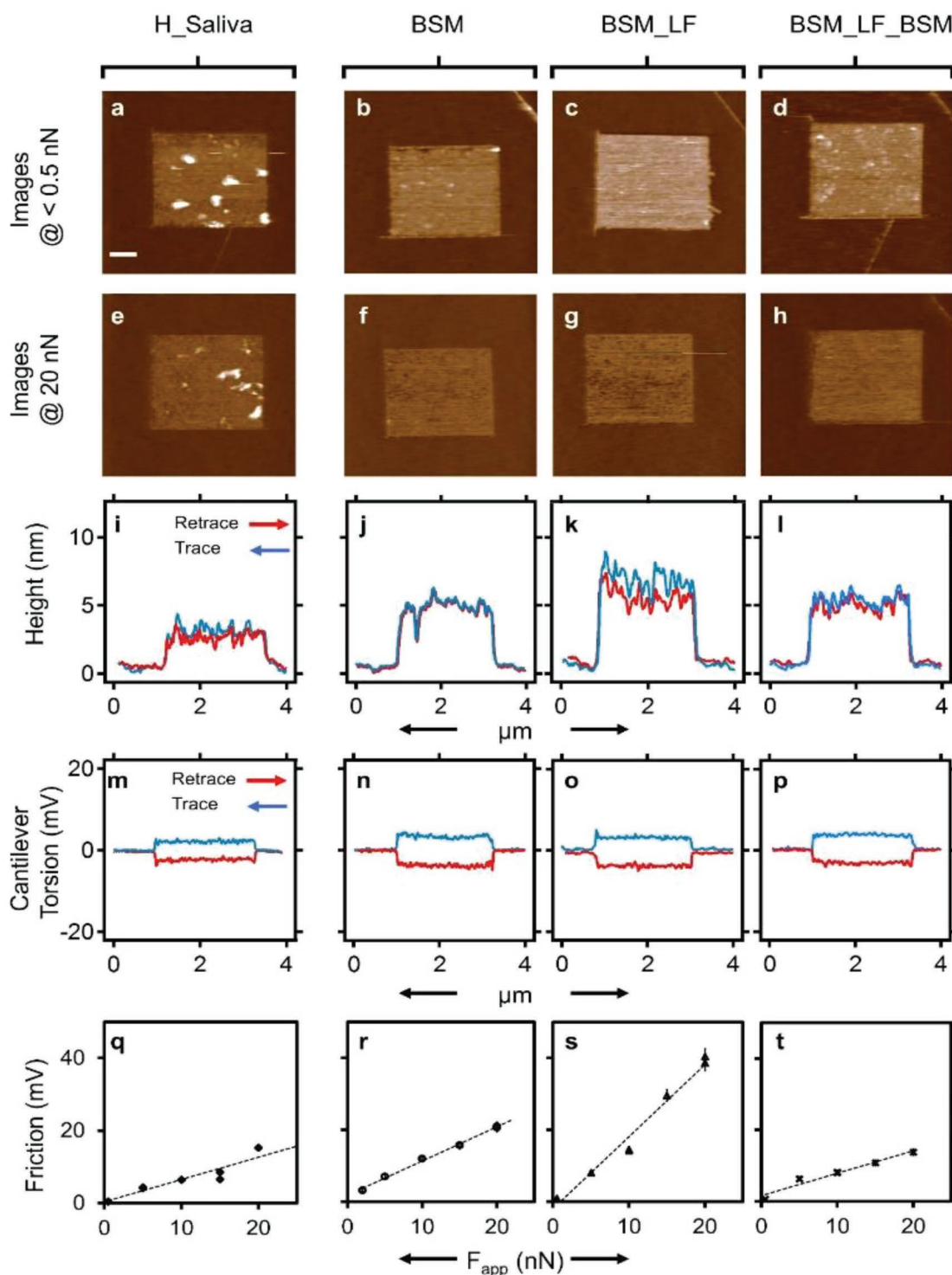


**Figure 6.** Height and lateral friction measurements of spatially confined human saliva, first layer BSM, BSM/LF network, and BSM/LF/BSM nanomatrices. a–d) The AFM topographic images of the respective proteins at normal force of 0.5 nN. e–h) The topographic images of the respective protein layers acquired at normal force of 20 nN. In the third i–l) and fourth row m–p), we have the trace/retrace height topographic profiles and the associated friction loop acquired at 5 nN. Lastly, q–t) show the plots of frictional force within a defined interval of applied normal force. Values are means  $\pm$  s.d. Scale bar; 500 nm. The scale bar is applicable to all the micrographs in this figure.

(see, e.g., the left-to-right trace in red and right-to-left trace in blue in Figure 6m–p), in which, however, the intensity of the lateral forces directly depends upon the AFM tip quality

and surface roughness in addition to the physicochemical properties of the surface and the applied force.<sup>[63–67]</sup> In our approach, we circumvented this issue by performing

side-by-side AFM imaging of nanografted patches, which consists in acquiring topographic and lateral force profiles containing a portion of TOEG-SAM (typically at the ends) and a portion of nanografted patch (typically in the center).<sup>[63]</sup> In this way, we measured changes in thickness and friction over the nanografted patches upon the adsorption of human saliva (Figure 6a,e,i,m,q), BSM (Figure 6b,f,j,n,r), BSM followed by LF (see BSM\_LF in Figure 6c,g,k,o,s) and a further BSM layer adsorbing on the initial BSM\_LF bilayer (see BSM\_LF\_BSM in Figure 6d,h,l,p,t), using TOEG-SAM as a topographic and chemical references under the very same AFM imaging conditions.

The AFM topography images shown in Figure 6a–d using a brighter-is-higher color code, were acquired in contact mode at a low force (at 0.5 nN) and demonstrate that BSM adsorption is specific on the positively charged patches, while the TOEG-SAM is substantially inert. Also, the roughness of the layer produced by human saliva (Figure 6a) is comparable to that of the BSM/LF binary models (Figure 6b–d), except for the presence of minor defects depicted by brighter features in Figure 6a, which are likely due to impurities and other salivary components in human saliva samples. Figure S17 in the Supporting Information shows the changes to the relative height of the positively charged monolayer patch measured at an applied force of 0.5 nN as the bilayer is formed over it, going from being nearly topographically indistinguishable from the surrounding TOEG-SAM to a height of approx. 5 nm for BSM alone and between 7 and 8 nm after the incubation of LF and the subsequent incubation of BSM. These topographic results suggest that BSM lay down flat on the positively charged patch as expected from the results described in Figure 4f, while LF forms a monolayer over the BSM. Also, at an applied force of 0.5 nN, the multilayer thickness saturates already after the addition of LF following the first BSM layer as the thickness of the BSM\_LF and BSM\_LF\_BSM systems is substantially the same despite the higher mass transfer involved in the formation of the latter. The result suggests that the addition of BSM over the BSM\_LF system leads to increased entanglement between BSM molecules on the surface not directly detectable by changes in topographic height.

As the force applied by the AFM tip increases to 5 nN, the BSM\_LF and BSM\_LF\_BSM exhibit very different mechanical properties as shown by the data in Figure 6. The profiles in Figure 6i–l show that the thickness of the bilayer system is substantially lower than that of the BSM\_LF system alone (see Figure 6k,l, respectively), whereas the friction levels for the two systems are substantially similar (see Figure 6o,p, respectively), and slightly higher than in the case of saliva (see Figure 6m). Also, the friction levels on the TOEG-SAM are much smaller than those measured over nanografted patches and identical (see, background in Figure 6m–p, data not shown). As the force increases to 20 nN, the topography of the BSM\_LF patches (see Figure 6g) reveals the presence of several topographic defects that are absent within the BSM\_LF\_BSM bilayer (see Figure 6h), thus evidencing a significant difference in layer compactness between the two systems.<sup>[65,67–69]</sup>

At such a higher applied force, nanoscale friction reveals well distinct behaviors for the investigated systems. The differential, friction values in the range 0.5–20 nN (see data in

Figures S18–S21, Supporting Information) reveal that the friction coefficient of the BSM\_LF\_BSM ( $0.64 \pm 0.07$  mV nN<sup>-1</sup>, see Figure 6q) is substantially identical to that of human saliva ( $0.62 \pm 0.11$  mV nN<sup>-1</sup>, see Figure 6q), while the higher values measured for BSM alone ( $1.0 \pm 0.04$  mV nN<sup>-1</sup>, see Figure 6r) and especially BSM\_LF ( $1.88 \pm 0.06$  mV nN<sup>-1</sup>, see Figure 6s) demonstrate that the bilayer system is structurally different than the other two examined experimental systems. Collectively, our differential, nanoscale analysis indicates that the bilayer system offers higher compressibility, compactness, and nanoscale lubrication than the BSM and BSM\_LF systems, which is compatible with a greater level of hydration in the bilayer resembling the performance of human saliva in QCM\_D results (Figure 4e–h, Figure S6, Supporting Information) and closely corroborating the macro and microscale lubrication behavior (Figures 2 and 3).

### 3. Discussion

The peculiar lubrication behavior of salivary pellicle is often considered to be the reasoning behind numerous biological functions, such as speech, oral and general health management, and food oral processing. One may assume that this would lead to saliva being well understood, and indeed, this is the case for salivary protein biochemistry enabling diagnosis of a range of infections and other systemic diseases. However, despite many decades of study, a detailed molecular understanding of the lubrication mechanism of saliva remains elusive. A true structural model of salivary lubrication must, at the very least, be able to emulate the physiologically low friction coefficient with known salivary protein components in their physiological configuration, which has not been achieved by any experimental study to date. Here, we combine lubrication measurements at macro to nanoscale with a range of complimentary techniques to fabricate a multilayer assembly using binary salivary proteins (highly glycosylated large-molecular weight anionic mucin and low molecular-weight cationic LF) for the first time to elucidate the true structural mechanism behind salivary lubrication.

In agreement with previous studies,<sup>[9,12,58,70]</sup> we demonstrate that the most commonly hypothesized lubricant, mucin by itself, cannot explain the low friction coefficients of real human salivary pellicle in the boundary regime. We discover that an electrostatically driven multilayered self-assembly of mucin with LF at physiological pH and ion conditions (pH 6.8) replicates the friction at interface, hydration, and degree of adsorption of human saliva across scales. This finding supports the assumption that adsorbed, nonmucin protein moieties are likely to play a predominant role in salivary lubrication.<sup>[9]</sup> The structure of salivary film would be rearranged under sliding into a mechanically more dense but rapidly-relaxing layer resulting in the dynamic lubrication, which is shown by both human saliva<sup>[58]</sup> and uniquely for the first time by the BSM/LF multilayered system in the present study. Combining together the experimental results of our macro, micro, and nanoscale analysis with real-time adsorption and dissipation, further supported by SCF calculations albeit for the equilibrium configuration of the adsorbed film, we propose a structural model based on the results that saliva creates a multilayer assembly, where LF acts as a “molecular glue” physically bringing together

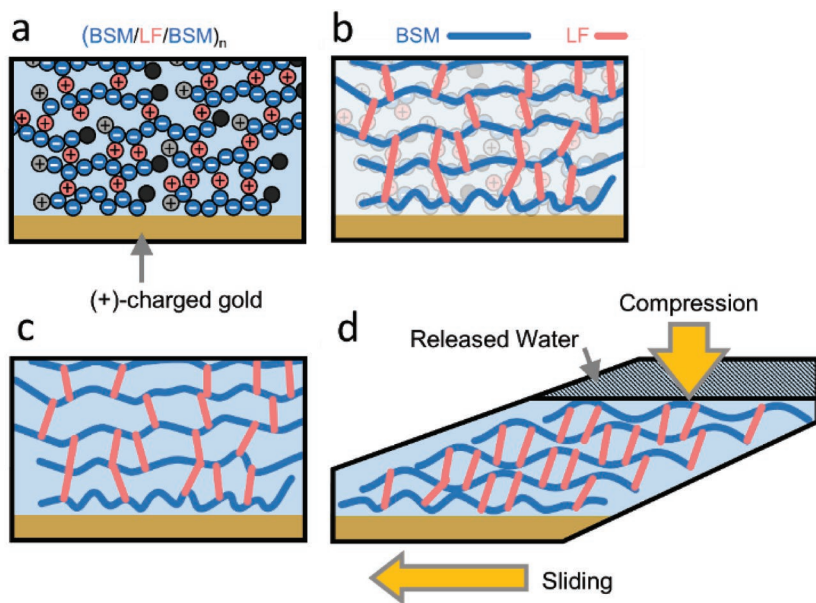


**Figure 7.** Lubrication mechanism for the saliva-like binary model. a) The layer-by-layer electrostatic self-assembly of BSM and LF on positively charged gold substrate obtained using QCM-D (a more opened format of Figure 4h), b,c) the conformational behavior of the network where LF forms the “molecular glues” between hydrated BSM–BSM network, and d) the behavior of this multilayered network on sliding that supports normal compressive forces, which being fluid-like can be sheared with minimal frictional dissipation.

the otherwise strongly repelling mucin–mucin polymers onto the surface, forming a mesh that traps water molecules to enable viscous lubrication with limited possible energy dissipation (see the diagram in Figure 7). The salivary pellicle can be considered as a heterogenous film, which consists of an anchoring sublayer and a hydrated outer layer.<sup>[50,71]</sup> Hence, LF is not only functionally relevant to bind more mucin polymers to form a porous scaffold for encapsulating water but LF also sneaks in through the porous mucin–substrate at the interface to aid boundary lubrication. The globular LF with a relatively small hydrodynamic diameter of 4–8 nm can fill the gaps between the asperities providing a “homogenizing effect” to the surface. In the boundary regime, where the asperities are in almost complete contact,<sup>[72]</sup> LF trapped within the gaps offering a smoother tribofilm during sliding causes a reduction in friction force. Thus, the role of LF at the surface can be also regarded as the grafting of positive charges enabling BSM–BSM network to bind to the surface, which is likely in case of real oral surfaces in human physiology. The strong affinity between surface and the BSM/LF system counteracts the energy dissipative process of lateral molecular movements.

Also, the multilayer replicates the behavior of saliva at a certain ion concentration highlighting the importance of electrostatic interaction in the salivary lubrication phenomena. In other words, as the ion concentration increases to a certain extent, the absolute values of the double-layer potential for mucin and LF approaching surfaces decrease. Also, ionic strength directly influenced the friction coefficients at macro to microscale, which suggests that the mucin/LF–surface interaction was also affected by ions such that less energy was dissipated.<sup>[73]</sup>

## 4. Conclusion

In conclusion, we designed an electrostatically driven multilayered self-assembly using salivary proteins mucin and non-mucinous LF that explains the molecular mechanism behind real human salivary lubrication performance. A delicate balance of the intrinsic electrostatic interactions of mucin and LF, hydrophobic interaction of LF with the surface, hydrogen bonding of mucin with water molecules, and extrinsic charge screening of this binary model by ions explains the superior lubrication as compared to singular salivary protein counterparts for the first time. More importantly, our experimental study supported by SCF theory highlights that low concentrations of small molecular positively charged proteins, such as LF in real human salivary pellicle act as “molecular glue” that catalyze mucin–mucin networking as well as mucin–surface binding. Such mucin–mucin networking facilitated by electrostatic interactions with small amounts of positively charged species allow creation of a nano-water reservoir encapsulating water via hydrogen bonding that provides the viscous fluid film lubrication. And the hydrophobic

attachment of the mucin to the surface facilitated by these low molecular weight species provides the effective boundary lubrication. Insights generated by our study bring new thinking for designing future nature-mimetic biolubricants, saliva substitutes for dry mouth, and therapies for oral infections associated with lubrication failure, as well as designing pleasurable nonfat food with biophysically informed lubricating mouthfeel to address global obesity challenges.

## 5. Experimental Section

**Materials:** All the protein solutions (LF and BSM) were prepared by dissolving in  $10 \times 10^{-3}$  M 4-(2-hydroxyethyl)-1-piperazineethanesulfonic acid (HEPES) buffer and adjusted to the human salivary pH (pH 6.8) and ions ( $1 \times 10^{-3}$  or  $10 \times 10^{-3}$  M NaCl) except for the zeta potential measurements. Zeta potential measurements was conducted using ultrapure water ( $18.2 \text{ M}\Omega\text{cm}$  resistivity) as the solvent. The LF was purchased from Ingredia (France) and used without any purification. Purification of BSM was conducted by dissolving BSM in ultrapure water at  $30 \text{ mg mL}^{-1}$  followed by dialysis in a 100 kDa molecular weight cut-off membrane (Spectrum Laboratories, USA) against ultrapure water for a week and lyophilized. The concentration of BSM solutions was  $1 \text{ mg mL}^{-1}$ , which was selected to set the mass ratio with LF. The mineral composition ( $\text{mg L}^{-1}$ ) analyzed using inductively coupled plasma mass spectrometry of the stock solutions was the following: purified BSM: Na 0.0510, Cu 0.0106, Zn 0.017, Mn < detection limit (0.000), Fe < detection limit (0.003), Mg 0.0240, Ca 0.1066, K < detection limit (0.081), P 0.019 and LF: Na 0.0331, Cu < detection limit (0.004), Zn 0.011, Mn < detection limit (0.000), Fe 0.146, Mg < detection limit (0.004), Ca < detection limit (0.018), K < detection limit (0.081), P 0.071. All other chemicals used in the experiments were purchased from Sigma-Aldrich without further purification unless otherwise specified.

**Human Saliva Collection:** Whole human saliva was collected from healthy and young female subjects ( $n = 15$ ) at 10 am, subjects were refrained from eating and drinking for at least 2 h before the saliva collection in accordance with the standard protocols of the University of Leeds Ethics Committee (MEEC 16-046). The collection of saliva required subjects with minimal oral movements and the saliva was collected at the same time of the days. After collection into pre-weighed chilled polypropylene tube, kept on ice, the human saliva was immediately diluted to 50% v/v in  $10 \times 10^{-3}$  M HEPES buffer, and then centrifuged at 3000 g for 3 min (centrifugation has limited influence on boundary lubricating property of adsorbed saliva<sup>[58]</sup>). The saliva samples were analyzed within 2 h of collection. The data were presented for one participant.

**Zeta-Potential:** Zeta-potentials of BSM, LF, and their mixtures at varying mass ratios, pH, and ions were measured in the standard folded capillary electrophoresis cells (DTS1070, using a Zetasizer Nano ZS instrument (Malvern Instruments Ltd., Worcestershire, UK). Each sample was measured in triplicates and each measurement was taken by the mean value of nine readings, and means and standard deviations were reported ( $n = 9 \times 3$ ) as shown in Figure S1 in the Supporting Information highlighting the charge complementarity of LF and BSM.

**Lubrication Measurements at Macroscale:** The lubricating properties of samples at macroscale were measured using a Mini Traction Machine (MTM2, PCS Instruments, London, UK) with PDMS (Sylgard 184, Dow Corning, Midland, MI, USA, base fluid and cross-linker (10:1 w/w)) ball ( $\varnothing$  19 mm)-on-disk ( $\varnothing$  46 mm) configuration, with surface roughness,  $R_a$  of 50 nm.<sup>[74]</sup> In addition, experiments were carried out using borosilicate glass ball-on-PDMS disk set up as schematically shown in Figure 1a to serve as a control for the tribopair surfaces used in the lubrication experiments at the microscale. The borosilicate glass balls ( $\varnothing$  19 mm) were purchased from PCS Instruments, London, UK. Tribopairs were immersed in protein solutions for an hour before the experiments. In contact mechanics, the Johnson–Kendall–Roberts (JKR) model of elastic contact provided an estimation to the contact dimensions and pressure when the role of adhesive forces between them was presumed to be relevant. Numerical expressions of the contact radius ( $a$ ) and maximum pressure ( $P_{\max}$ ) for an elliptical contact in the JKR theory are introduced in Equations (2) and (3), respectively

$$a^3 = \frac{3R}{4E^*} \left( F_N + 6\gamma\pi R + \sqrt{12\gamma\pi R F_N + (6\gamma\pi R)^2} \right) \quad (2)$$

$$P_{\max} = \frac{2aE^*}{\pi R} - \left( \frac{4\gamma E^*}{\pi a} \right)^{0.5} \quad (3)$$

here  $R$  is the sphere radius and  $E^* = \left( \frac{1-\nu'^2}{E'} + \frac{1-\nu''^2}{E''} \right)^{-1}$  is the reduced Young's modulus of the contact surface, with  $\nu'$  and  $\nu''$  representing the Poisson's ratio, the  $E'$  and  $E''$  representing and Young's moduli of each of the two surfaces. From Equation (3), it was evident that the contact pressure had two contributions. The first term on the right-hand side represented the contribution from normal force ( $F_N$ ), while the second one was the contribution from the adhesive forces, quantified by the adhesion energy ( $\gamma$ ). Due to the large normal forces involved in the MTM experiments ( $F_N = 2$  N), contribution from adhesive forces was commonly considered to be negligible and hence was discarded. Thus, in the case of the PDMS ball-on-disk tribological set-up ( $E^* \sim 1.6$  MPa,  $a \sim 0.002$  m), the calculated  $P_{\max}$  was 222.2 kPa.<sup>[8]</sup> In case of the glass-on-PDMS contact ( $E^* \sim 3.0$  MPa,  $a \sim 0.002$  m),  $P_{\max}$  was 343 kPa. Operational range of loads ( $F_N$ ) for the MTM when working with soft complaint surfaces covered from 0.5 to 5.0 N, impacting contact pressure ( $\approx F_N^{1/3}$ ) only by a factor of 2.1. Thus, this load range was also likely to have limited impact on the attainable friction coefficients ( $F_N^{-0.55}$ ) with a maximum factor of 3.0, as was observed elsewhere.<sup>[75]</sup> For this reason, experiments in the macroscale (MTM) were carried out at a fixed load of 2.0 N, which was commonly used in the literature to describe the contribution of tribology in the oral processing.<sup>[76,77]</sup> The sliding speeds were varied from low ( $0.001$  m s<sup>-1</sup>) to high ( $0.500$  m s<sup>-1</sup>) as well as from high-to-low. An MTM

glass lid was used to maintain the samples at the ambient temperature (25 °C), to avoid evaporation. Data were only reported from high-to-low speeds, as the Stribeck curves showed negligible hysteresis. The sliding to rolling ratio,  $SRR = |U' - U''|/\bar{U}$  was maintained at 0.5, where  $U'$  and  $U''$  were the speeds of the ball and disk, respectively, and the entrainment speed was defined as  $\bar{U} = \frac{1}{2}(U' + U'')$ . Prior to each test, the surfaces were cleaned with acetone and rinsed with Milli-Q water. One ball-and-disk pair was used each time for an individual experiment and then discarded.

**Lubrication Measurements at Microscale:** Microtribometry methods were employed to measure friction forces of the adsorbed films at the microscale. The friction behaviors of the films were measured using a reciprocating pin-on-plate microtribometer (NTR3, Anton Paar, UK). A boro-silicate glass-PDMS tribopair was used for these experiments. The PDMS disks were prepared by mixing the base and cross-linker (10:1 w/w) of a Sylgard 184 elastomer kit (Dow Corning, Midland, MI, USA), vacuuming to remove air bubbles and curing overnight at 70 °C, followed by casting using a smooth stainless steel mold. The counter surface was a boro-silicate glass lens with a spherical radius,  $R = 6.2$  mm and  $R_a = 2$  nm. The PDMS disk ( $R = 5$  mm and  $R_a = 50$  nm) was disposable, whereas the glass-pin was used after cleaning with ethanol and ultrapure water.

Prior to sliding, the PDMS surfaces were immersed in 1 mL of protein solutions or human saliva for an hour and rinsed by their initial buffer solutions. This was followed by rinsing with their initial buffer solutions. For the experiments with BSM-LF multilayers, sequential adsorption of the proteins to 2.5 bilayers (BSM/LF/BSM/LF/BSM) denoted as (BSM/LF/BSM)<sub>2.5</sub> was used, and this multilayered architecture on PDMS sensor was obtained from the QCM-D chamber (discussed in details in the QCM-D) section. Tribological assessment was performed along the linear path with the amplitude of 500  $\mu$ m and at the fixed sliding speed of 1 mm s<sup>-1</sup>, schematically shown in Figure 1b. To assess load-bearing characteristics of the films, the normal force was increased incrementally in the range of 1 to 10 mN ( $P_{\max}$  values were 89.0 up to 104.0 kPa,  $R = 0.00042$ – $0.00046$  m,  $\gamma = 0.2$  J m<sup>-2</sup>, calculated using Equations (2) and (3)) and the resultant friction forces were continuously measured over 50 cycles under each load at a frequency of 400 Hz. All the tribology tests were carried out at an ambient temperature (25 °C) in triplicate to ensure the reproducibility of the recorded results.

**AFM Instrumentation:** All AFM experiments (starting from imaging, nanografting, thickness, and lateral friction measurements of LF, BSM, and other possible protein sandwiches) were carried out with MFP-3D-AFM (Standalone) (Asylum research, Santa Barbara, CA). For nanografting, commercially available pyramidal silicon etched probes NSC 18/no Al of spring constant of 2.3 N m<sup>-1</sup> were used as stated by the manufacturer (Mikro-Masch, Germany). For contact mode imaging and normal spring constant calibration-soft probe (CSC 38/no Al), normal spring constant ( $K_n$ ) (in-house calibration) of 0.03–0.09 N m<sup>-1</sup>, (Mikro-Masch, Germany) was used.

**Preparation of Ultra-Flat Gold Substrate:** Ultra-flat gold substrates were prepared using sequential deposition of gold via electron beam evaporation. First, gold was deposited at the rate 0.05 nm s<sup>-1</sup> until a film of 5 nm was obtained, then the rate of evaporation was increased to 0.1 nm s<sup>-1</sup>, until a 100 nm thick film was formed on the freshly cleaved mica (Mica New York Corp., clear ruby muscovite) at 10<sup>-6</sup> mbar, at room temperature. The planar gold sheet of (111) crystallographic plane obtained on mica was sliced into few millimeter squares (approximately 5  $\times$  5 mm<sup>2</sup>) in area using Stanley-199 blade. To transfer the ultra-flat gold surface from mica to the polished side of smaller squares (smaller than sliced gold on a mica sheet) p-doped silicon wafers, a drop of SU-8 photoresist adhesive (negative tone photoresist, MicroChem, USA) was evenly dispensed on the polished side of silicon. Then, a sandwich of silicon-gold-mica was obtained by impressing the polished section of silicon on the gold section of mica. All silicon-gold-mica sandwich squares were cured at 130 °C for at least 48 h. The samples were cooled down to room temperature without any external cooling system and this was done to avoid thermal stresses that could result in gold film detachment from the mica substrate. Without any further surface

treatment, the samples were stored at room temperature, ready to be used for self-assembled monolayer preparation.

**Preparation of Top-Oligo-Ethylene-Glycol SAM (TOEGSAM) on the Ultra-Flat Gold Substrate:** An ultra-flat gold surface was obtained from silicon-gold-mica sandwich by mechanical stripping the mica substrate from the silicon-gold-mica sandwich. This was immersed and incubated in the solution of  $100 \times 10^{-6}$  M of top-oligo-ethylene glycol (TOEG-6 (HS-((CH<sub>2</sub>)<sub>11</sub>)-(O-CH<sub>2</sub>-CH<sub>2</sub>)<sub>6</sub>-OH), Prochimia and Sigma Aldrich) in absolute ethanol and 1 M NaCl, TE1X, for 6 h. After the incubation time, serial rinsing was performed first in ethanol and then in 1 M NaCl, TE1X ( $10 \times 10^{-3}$  M Tris,  $1 \times 10^{-3}$  M EDTA) buffer. This was to remove any physically adsorbed contaminants. The TOEG monolayer then served as bio-repellent for a specific adsorption of protein onto the surface.

**Nanografting of Amino-Terminated Undecanethiol within TOEG-Passivated Gold Substrate:** First, TOEG passivated gold substrate was adhered to the homemade liquid cell and was transferred onto the X-Y base plate of the AFM scanner. Next,  $100 \times 10^{-6}$  M solution of 11-amino-1-undecanethiol hydrochloride (HS-((CH<sub>2</sub>)<sub>11</sub>)-NH<sub>2</sub>HCl) was dispensed on the sample and a fast imaging was performed in tapping mode. This allowed us to have a survey of the surface and select a flat and clean section for nanografting. Afterward, the AFM mode was changed to contact mode and  $2 \times 2 \mu\text{m}^2$  scan area was selected at  $\approx 120$  nN with scan angle of  $90^\circ$  for the grafting process. The grafting process aided the selective replacement of the prior TOEG molecules with the amino-terminated undecanethiol molecules. After grafting process, a  $20 \times 20 \mu\text{m}^2$  section that contained the grafted patches was scanned at very low force (high set point) in tapping mode.

**Layer-by-Layer Adsorption of BSM and LF:** The leftover solution of amino-terminated undecanethiol was removed and the sample was rinsed twice with  $10 \times 10^{-3}$  M NaCl-HEPES buffer of pH 6.8. Next, the sample was incubated with 100  $\mu\text{L}$  solution of 1 mg mL<sup>-1</sup> of BSM at 25 °C for an hour. And then the topographic images of laterally confined BSM were acquired. To form the BSM/LF composite, the solution of 1 mg mL<sup>-1</sup> of LF was added and allowed to adsorb for an hour at 25 °C. Afterward, the second set of topographic images was performed in the protein-free  $10 \times 10^{-3}$  M NaCl-HEPES buffer. Lastly, to form the bilayer, i.e., BSM\_LF\_BSM, the second solution of BSM (1 mg mL<sup>-1</sup> in  $10 \times 10^{-3}$  M NaCl-HEPES) was added and allowed to adsorb onto the LF-terminated nanopatches, the adsorption lasted for an hour at 25 °C. And then the final round of imaging was performed in contact mode within protein-free  $10 \times 10^{-3}$  M NaCl-HEPES, this yielded the topographic images of the confined BSM/LF/BSM nanopatches.

**Lateral Force Microscopy of Multilayered Proteins at Nanoscale:** Prior to lateral/friction measurements at nanoscale (Figure 1c), force-distance curve calibration was performed in contact mode on the TOEG passivated substrate, within  $10 \times 10^{-3}$  M NaCl-HEPES buffer solution. This allowed the software to estimate the cantilever deflection inverse optical lever sensitivity, which was required to calculate the normal spring constant. The values estimated for normal spring constant were 0.03–0.09 N m<sup>-1</sup>. The procedure used for the force-distance measurement can be found in the Asylum MFP-3D operational manual. Next, spatially confined protein layers were imaged at different applied normal force (1–20 nN) and the associated frictional loops (both trace and retrace) were acquired. Each measurement was repeated at least three times for the reliability and reproducibility of the frictional loops using the newly generated spatially confined proteins at each experimental section. Next, Igor Pro 6.37A was used to transpose the friction loop into the profile that represented the difference of trace and retrace waves associated with each friction loop. Also, the same software was used for image processing and data analysis. Note, torsional spring constant was not estimated because it was difficult to estimate the cantilever tip radius when it was fully in contact with the sample, as such the frictional forces were reported in milli-Volt (mV) and not in Newton (N). The aforementioned procedural steps were used to characterize spatially confined BSM, BSM\_LF, and BSM\_LF\_BSM nanomatrices.

**QCM-D:** The real-time multilayer assembly behavior was measured by QCM-D (E4 system, Q-Sense, Sweden) as shown in Figure 1d. Upon the adsorption of protein films on the substrates, this device

had the capacity to simultaneously measure the shifts in frequency and dissipation at different overtones to provide wealthy information on the adsorption properties and thickness of the layers. To investigate the effect of surface chemistry on the multilayered film formation, the hydrophilic gold-covered sensor (QSX-301, Q-Sense), hydrophobic PDMS-coated sensor (QSX-999, Q-Sense), and positively charged amine-terminated gold-covered sensors were used. To date, PDMS-coated sensor represented a better approximation for human oral surfaces as compared to conventional gold sensors.<sup>[8]</sup> The positively charged gold-coated sensors were fabricated by incubating the gold sensors in  $1 \times 10^{-3}$  M amino-terminated EG thiol (HS-C<sub>11</sub>-NH<sub>3</sub><sup>+</sup>Cl<sup>-</sup>) solution overnight, followed by rinsing and 2 min sonication in ethanol to remove any nonspecifically bound material.

Prior to the experiments, the gold sensors were cleaned for 10 min under UV/ozone, followed by sonication in a 2% w/w sodium dodecyl sulfate solution for 15 min, sonication in ultrapure water for 15 min, and 10 min under UV/ozone. Positively charged sensors were used after rinsing with ethanol and drying with nitrogen gas. The PDMS surfaces were cleaned by 30 s immersion in toluene, followed by 30 s immersion in isopropanol, then 2 min immersion in ultrapure water, drying with nitrogen gas and letting the remaining solvent molecules to evaporate for 2 h. All the solutions were supplied into QCM-D chamber by a peristaltic pump with a flow rate of 100  $\mu\text{L min}^{-1}$  at 25 °C. The first step was to inject the buffer solution until a stable baseline was observed. Subsequently, the layer-by-layer formation was conducted by manually alternating the individual salivary protein solutions. The BSM and LF were injected in the system and left to adsorb for 45 min under the flow conditions, followed by 45 min of rinsing in buffer solution. For the adsorption of premix protein solutions and human saliva, solutions were injected into the system for at least an hour, allowing the system to equilibrate, followed by rinsing in buffer solutions. All the sensors were used only for one sample and disposed after one experiment.

The data were fitted using Voigt model for viscoelastic solids (namely, “Smartfit Model”) by Dfind (Q-Sense, Sweden) software to obtain the mass and thickness of the hydrated protein layers. The 3rd to 11th overtones were taken into account for data analyzing (see Table S3 in the Supporting Information for densities). The nomenclature for each multilayer system followed the usual convention (polymer A/polymer B)<sub>n</sub>, where polymer A and polymer B refer to the salivary proteins used in the assembly process and *n* is the number of bilayers deposited.

**Contact Angle Measurement:** The static water-contact angles were measured using a drop-shape analysis device (OCA 25, Dataphysics UK). Nearly 5  $\mu\text{L}$  of ultrapure water dispensed by the computer-controlled automatic liquid system was placed on the surfaces. The averaged angle was then determined by the values of the right and left contact angles of the droplet, which was estimated from the image observed by the digital camera. After film formation in QCM-D, the multilayered (BSM/LF/BSM)<sub>4.5</sub> films on the PDMS-coated sensor were taken out of the QCM-D device and kept in the temperature-controlled chamber (temperature set at 25 °C) to be air-dried. To minimize the influence of salt on the contact angle measurements, only the experiments with buffer containing  $1 \times 10^{-3}$  M NaCl and human saliva diluted with the salt-free buffer were presented in this study. The temperature of the experiments was set at 25 °C to reduce the droplet evaporation. Each measurement was performed in triplicate at different locations on the surfaces.

**cryo-SEM:** A cryo-SEM (FEI Quanta 200F FEG ESEM, Japan) was used to study the structural features of the individual proteins and multilayered (BSM/LF/BSM)<sub>4.5</sub> films on the gold surface derived from the QCM-D chamber. All the samples were first loaded onto the rivet sample holders and frozen in liquid nitrogen, then transferred into the preparation chamber at high vacuum ( $<10^{-7}$  m bar) and low temperature (−14 °C). The top rivet was removed, revealing a freeze-fractured surface that was sublimed at −90 °C for 3 min inside the pre-chamber. The samples were visualized at 1 kV after Pt-coating (5.0 mA for 45 s).

**SCF Calculations:** In order to theoretically investigate the interaction energies and equilibrium volume fraction profiles of the LF and BSM

species that are uniformly adsorbed onto two planar hydrophobic surfaces, the well-known Scheutjens–Fleer SCF theory<sup>[59,60]</sup> was applied to this problem. The theory has widely been used to understand the adsorption of polymers including disordered proteins, as well as behavior of protein–protein<sup>[78]</sup> and protein–polysaccharide mixed or multilayered systems<sup>[79–81]</sup> at interfaces. Details of the model for protein-like chains is available elsewhere<sup>[60]</sup> and will not be reproduced here but rather a brief summary is provided specific to this study. The space between the planar surfaces was divided into equidistant layers with lattice layer thickness set at  $a_0 = 3 \text{ \AA}$  (nominal size of a peptide bond). Each lattice site could be occupied by a polymer residue of either LF or BSM chains, water molecules, or ions such as  $\text{Na}^+$ ,  $\text{Cl}^-$ , etc., so that total volume fraction for all the species in each lattice layer adds up to equal 1.

The amino acid residues of LF or BSM were grouped into five sets based on the hydrophobicity, polarity, ability to get ionized or electrically charged.<sup>[82,83]</sup> Obtaining the variation in the volume fraction profiles, i.e.,  $\phi_i^\alpha(z)$  of LF, BSM on their own as well as in (BSM/LF/BSM)<sub>n</sub>, along the z-direction perpendicular to the surfaces, for each of the segment type  $\alpha$ , belonging to each molecules species (LF or BSM)  $i$ , was the primary goal of the SCF calculations. The segment potential  $\psi^\alpha(z)$ , i.e., the potential experienced by a particular segment type  $\alpha$ , at a layer distance  $z$  from one of the surfaces was also calculated for LF or BSM on its own (as well as in the mixed system) from summation of three separate components as shown below in Equation (4)

$$\psi^\alpha(z) = \sum_i \sum_\beta \chi_{\alpha\beta} \left( \phi_i^\beta(z) - \Phi_i^\beta \right) + q_\alpha \psi_{\text{elec}}(z) + \psi_{\text{hd}}(z) \quad (4)$$

where bulk concentration of the monomer of type  $\beta$ , belong to either of LF or BSM species  $i$ , is denoted by  $\Phi_i^\beta$ . The first component represented a short-range nonelectrostatic contribution described by Flory–Huggins interaction parameter,  $\chi_{\alpha\beta}$ . Hydrophobic segments had strong adsorption affinities for the surface ( $\chi = -2 k_B T$ ) but repel water, ions, and also polar segments ( $\chi = +2.5 k_B T$ ), polar segments had affinity for water ( $\chi = 0 k_B T$ , representing an athermal solvent) and the interactions between water and ions were represented by  $\chi = -1 k_B T$ <sup>[78,80]</sup> favoring hydration of ions, where  $k_B$  is Boltzmann constant and  $T$  is the temperature. The second term in Equation (4) involved the long-range (electrostatic) potential  $\psi_{\text{elec}}(z)$ , where particular segment type  $\alpha$  has charge  $q_\alpha$ , calculated using its  $\text{pK}_a$  value for the ionizable amino acid groups (e.g.,  $\approx 4.5$  for the set representing acidic amino acids such as Asp, Glu, and end-COOH; 10 for the group containing the basic amino acids such as Arg, Lys, and end-NH<sub>2</sub>; and 6.75 for His) and pH of the bulk solution. The third term in Equation (4) was a hard-core potential  $\psi_{\text{hd}}(z)$  ensuring that each layer was filled with the LF or BSM or ions or water (i.e., was not left empty) and was the same for any species within a given lattice layer.

In order to find both quantities,  $\phi^\alpha(z)$  and  $\psi^\alpha(z)$ , a set of nonlinear equations was solved self-consistently by an iterative procedure to achieve convergence. The procedure could also be shown to amount to minimization of the free energy of the system with respect to the volume fraction variation of all species in the system away from the surface. The net interaction energy,  $A(D) = A_T(D) - A_T(\infty)$ , where  $A_T(D)$  is the free energy at surface–surface separation of  $D$ , measured in units of  $k_B T$  per lattice site (energy/area) was calculated as described previously<sup>[84]</sup> and obtained here for LF and BSM on their own. Segment density profiles were compared for LF and BSM on their own and when they were present in the multilayered system (BSM/LF/BSM)<sub>n</sub> using a separation distance of 70 monomer units between two planar surfaces, i.e., a gap size of 21 nm.

For modeling LF and BSM, the amino acid residue sequence of bovine LF (F2FB42) and bovine salivary mucin (MUC5B, B9VPZ5) was obtained from UniProt Protein Data Bank (<http://www.uniprot.org>). The LF and BSM were consisted of 708 residues and 6724 residues, respectively. All the amino acids in this model were divided into five groups according to their properties: hydrophobic (Ala, Val, Leu, Ile, Met, Trp, Phe, Pro, Cys); polar (Ser, Thr, Tyr, Asn, Gln), ‘G’ (Gly); basic (Arg, Lys, His); and acidic (Glu, Asp). It was seen that this classification

resulted in LF roughly consisting of four large blocks, made up of mostly hydrophobic–hydrophilic–hydrophobic–hydrophilic residues, when counting from the N-terminal corroborating the conformation in literature<sup>[36]</sup> where one had two distinct hydrophobic globules joined together by a hydrophilic train, as well as a relatively hydrophilic tail on the C-terminus side.

In order to emphasize the specific properties of the mucin, a simplified BSM model was designed that consisted of 30 amino acid from each of the C- and N-terminal with a middle hydrophilic and uniformly charged section consisting of 2000 residues. This middle segment was to represent the large glycoside hydrophilic section of BSM. The charge of mucin was estimated to be  $\approx -202e$ , from zeta potential (see Figure 1b, Supporting Information) using a representative value for charge as obtained in between the two extremes of Smoluchowski and Hückel approximation, with corresponding radius of gyration ( $R_g$ ) taken to be 35 nm for BSM, as given in literature.<sup>[85]</sup> The assumption of charge distribution in BSM was that the charge in the two ends was calculated and any additional charge was attributed equally to the glycoside hydrophilic residues in between. Calculations were done for a relatively large surface–surface separation of 84 nm (280 monomer units) for LF and BSM and also for close separation of 21 nm (corresponding to a distance of 70 monomer units). For both LF and BSM, SCF calculation programs were run at remaining protein bulk volume fractions of  $1 \times 10^{-7}$ , as it was assumed that most of the protein in the system could be adsorbed to the surface. The volume fraction of ions (assumed monovalent for both positive and negative ones) was set at 0.002 (roughly equivalent to  $10 \times 10^{-3} \text{ M NaCl}$ ) at neutral pH. To the best of our knowledge this was the first study that used SCF to understand LF–BSM interactions.

**Statistical Analysis:** Data were presented in term of mean value and standard deviation (SD) of at least three independent readings of at least three independent experiments ( $n = 3 \times 3$ ) unless otherwise stated and data were statistically analyzed using SPSS. One-way analysis of variance with follow-up Tukey’s (every group compared to every other group) multiple comparisons test was employed to determine significant differences among multiple groups (see Tables S2 and S3 in the Supporting Information).

## Supporting Information

Supporting Information is available from the Wiley Online Library or from the author.

## Acknowledgements

This study has received funding from the European Research Council (ERC) under the European Union’s Horizon 2020 research and innovation program (grant agreement no. 757993). The authors thank Stuart Micklethwaite (LEMAS – Leeds Electron Microscopy and Spectroscopy Centre, Faculty of Engineering, University of Leeds) for his technical support in electron microscopy.

## Conflict of Interest

The authors declare no conflict of interest.

## Author Contribution

A.S. designed the research, experimental protocol, and supervised the project. F.X. performed the microtribology experiments and did data analysis, M.B. aided in designing these experiments at microscale and data analysis. F.X. and E.A.-R. performed the macro-tribology experiments

and did the data analysis. F.X. and E.L. performed all the QCM-D experiments and did the data analysis, and T.C. aided in the QCM-D data analysis. E.L. organized the protein bank data and R.E. designed the SCF numerical simulations, ran the analysis, and interpreted the theoretical data. M.C. designed the AFM experiments, aided in data analysis and discussions. A.A. performed the AFM experiments, interpreted, and analyzed the data. A.S. wrote the manuscript with inputs from all authors. A.S. had primary responsibility for final content; and all authors read, edited, and approved the final manuscript.

## Keywords

aqueous lubrication, mucin, multilayer, nanografting, self-assembly

Received: September 10, 2019

Published online: November 20, 2019

- [1] M. R. Panman, B. H. Bakker, D. den Uyl, E. R. Kay, D. A. Leigh, W. J. Burma, A. M. Brouwer, J. A. J. Geenevasen, S. Woutersen, *Nat. Chem.* **2013**, *5*, 929.
- [2] Y. Diao, R. M. Espinosa-Marzal, *Nat. Commun.* **2018**, *9*, 2309.
- [3] L. Ma, A. Gaisinskaya-Kipnis, N. Kampf, J. Klein, *Nat. Commun.* **2015**, *6*, 6060.
- [4] S. Jahn, J. Klein, *Macromolecules* **2015**, *48*, 5059.
- [5] G. H. Carpenter, *Annu. Rev. Food Sci. Technol.* **2013**, *4*, 267.
- [6] M. Cárdenas, U. Elofsson, L. Lindh, *Biomacromolecules* **2007**, *8*, 1149.
- [7] J. Vinke, H. J. Kaper, A. Vissink, P. K. Sharma, *Sci. Rep.* **2018**, *8*, 9087.
- [8] A. Sarkar, E. Andablo-Reyes, M. Bryant, D. Dowson, A. Neville, *Curr. Opin. Colloid Interface Sci.* **2019**, *39*, 61.
- [9] I. C. Hahn Berg, L. Lindh, T. Arnebrant, *Biofouling* **2004**, *20*, 65.
- [10] A. Ash, G. R. Burnett, R. Parker, M. J. Ridout, N. M. Rigby, P. J. Wilde, *Colloids Surf., B* **2014**, *116*, 603.
- [11] T. Baumann, R. Bereiter, A. Lussi, T. S. Carvalho, *Sci. Rep.* **2017**, *7*, 12999.
- [12] G. E. Yakubov, L. Macakova, S. Wilson, J. H. C. Windust, J. R. Stokes, *Tribol. Int.* **2015**, *89*, 34.
- [13] A. Sarkar, F. Xu, S. Lee, *Adv. Colloid Interface Sci.* **2019**, *273*, 102034.
- [14] M. Bossola, L. Tazza, *Nat. Rev. Nephrol.* **2012**, *8*, 176.
- [15] F. Xu, L. Laguna, A. Sarkar, *J. Texture Stud.* **2019**, *50*, 27.
- [16] Z. Liu, Y. Jiao, Y. Wang, C. Zhou, Z. Zhang, *Adv. Drug Delivery Rev.* **2008**, *60*, 1650.
- [17] M. Dodds, S. Roland, M. Edgar, M. Thornhill, *BDJ Team* **2015**, *2*, 15123.
- [18] J. R. Stokes, M. W. Boehm, S. K. Baier, *Curr. Opin. Colloid Interface Sci.* **2013**, *18*, 349.
- [19] A. Singh, M. Corvelli, S. A. Unterman, K. A. Wepasnick, P. McDonnell, J. H. Elisseeff, *Nat. Mater.* **2014**, *13*, 988.
- [20] S. Lee, N. D. Spencer, *Science* **2008**, *319*, 575.
- [21] J. Seror, L. Zhu, R. Goldberg, A. J. Day, J. Klein, *Nat. Commun.* **2015**, *6*, 6497.
- [22] X. Zhang, J. Wang, H. Jin, S. Wang, W. Song, *J. Am. Chem. Soc.* **2018**, *140*, 3186.
- [23] A. Dedinaite, P. M. Claesson, *Phys. Chem. Chem. Phys.* **2017**, *19*, 23677.
- [24] N. Nikogeorgos, P. Efler, A. B. Kayitmazer, S. Lee, *Soft Matter* **2015**, *11*, 489.
- [25] O. Svensson, L. Lindh, M. Cárdenas, T. Arnebrant, *J. Colloid Interface Sci.* **2006**, *299*, 608.
- [26] M. Sakai, T. Matsushita, R. Hoshino, H. Ono, K. Ikai, T. Sakai, *Sci. Rep.* **2017**, *7*, 9753.
- [27] L. Laguna, A. Sarkar, *Tribol.-Mater., Surf. Interfaces* **2017**, *11*, 116.
- [28] N. M. Harvey, G. E. Yakubov, J. R. Stokes, J. Klein, *Biomacromolecules* **2011**, *12*, 1041.
- [29] J. H. H. Bongaerts, K. Fourtouni, J. R. Stokes, *Tribol. Int.* **2007**, *40*, 1531.
- [30] C. Liu, E. Thormann, E. Tyrode, P. M. Claesson, *J. Colloid Interface Sci.* **2015**, *443*, 162.
- [31] N. Nikogeorgos, J. B. Madsen, S. Lee, *Colloids Surf., B* **2014**, *122*, 760.
- [32] J. An, C. Jin, A. Dédinaite, J. Holgersson, N. G. Karlsson, P. M. Claesson, *Langmuir* **2017**, *33*, 4386.
- [33] S. Lee, *World Acad. Sci., Eng. Technol.* **2013**, *75*, 1094.
- [34] L. Macakova, G. E. Yakubov, M. A. Plunkett, J. R. Stokes, *Colloids Surf., B* **2010**, *77*, 31.
- [35] E. Adal, A. Sadeghpour, S. Connell, M. Rappolt, E. Ibanoglu, A. Sarkar, *Biomacromolecules* **2017**, *18*, 625.
- [36] H. M. Baker, E. N. Baker, *Biochem. Cell Biol.* **2012**, *90*, 320.
- [37] A. Sarkar, K. K. T. Goh, H. Singh, *Food Hydrocolloids* **2009**, *23*, 1270.
- [38] L. Lindh, I. E. Svendsen, O. Svensson, M. Cárdenas, T. Arnebrant, *J. Colloid Interface Sci.* **2007**, *310*, 74.
- [39] J. Ahn, T. Crouzier, K. Ribbeck, M. F. Rubner, R. E. Cohen, *Biomacromolecules* **2015**, *16*, 228.
- [40] S. P. Authimoolam, A. L. Vasilakes, N. M. Shah, D. A. Puleo, T. D. Dziubla, *Biomacromolecules* **2014**, *15*, 3099.
- [41] O. Svensson, T. Arnebrant, *Curr. Opin. Colloid Interface Sci.* **2010**, *15*, 395.
- [42] G. Decher, *Science* **1997**, *277*, 1232.
- [43] R. Bansil, B. S. Turner, *Curr. Opin. Colloid Interface Sci.* **2006**, *11*, 164.
- [44] S. Block, O. Soltwedel, P. Nestler, C. A. Helm, in *Multilayer Thin Films: Sequential Assembly of Nanocomposite Materials*, Vol. 1, 2nd ed. (Eds: G. Decher, J. B. Schlenoff), Wiley-VCH Verlag GmbH & Co. KGaA, Weinheim, Germany **2012**, p. 269.
- [45] T. Crouzier, C. H. Beckwith, K. Ribbeck, *Biomacromolecules* **2012**, *13*, 3401.
- [46] T. Saارين, M. Österberg, J. Laine, *Colloids Surf., A* **2008**, *330*, 134.
- [47] G. Ladam, P. Schaad, J. C. Voegel, P. Schaaf, G. Decher, F. Cuisinier, *Langmuir* **2000**, *16*, 1249.
- [48] Z. Feldötö, T. Pettersson, A. Dédinaite, *Langmuir* **2008**, *24*, 3348.
- [49] L. Shi, K. D. Caldwell, *J. Colloid Interface Sci.* **2000**, *224*, 372.
- [50] D. H. Veeregowda, H. J. Busscher, A. Vissink, D. J. Jager, P. K. Sharma, H. C. van der Mei, *PLoS One* **2012**, *7*, e42600.
- [51] J. B. Madsen, J. Sotres, K. I. Pakkanen, P. Efler, B. Svensson, M. Abou Hachem, T. Arnebrant, S. Lee, *Langmuir* **2016**, *32*, 9687.
- [52] D. P. Chang, N. I. Abu-Lail, F. Guilak, G. D. Jay, S. Zauscher, *Langmuir* **2008**, *24*, 1183.
- [53] T. Sun, G. Han, M. Lindgren, Z. Shen, A. Laaksonen, *Biomater. Sci.* **2014**, *2*, 1090.
- [54] M. Lundin, T. Sandberg, K. D. Caldwell, E. Blomberg, *J. Colloid Interface Sci.* **2009**, *336*, 30.
- [55] L. Lindh, P. O. Glantz, I. Carlstedt, C. Wickström, T. Arnebrant, *Colloids Surf., B* **2002**, *25*, 139.
- [56] N. Vassilakos, T. Arnebrant, P. O. Glantz, *Scand. J. Dent. Res.* **1992**, *100*, 346.
- [57] J. B. Schlenoff, in *Multilayer Thin Films*, Vol. 1 (Eds: G. Decher, J. B. Schlenoff), Weinheim, Germany **2012**, p. 281.
- [58] N. M. Harvey, G. E. Yakubov, J. R. Stokes, J. Klein, *Biofouling* **2012**, *28*, 843.
- [59] J. M. H. M. Scheutjens, G. J. Fleer, *J. Phys. Chem.* **1979**, *83*, 1619.
- [60] J. M. H. M. Scheutjens, G. J. Fleer, *J. Phys. Chem.* **1980**, *84*, 178.
- [61] F. Bano, L. Fruk, B. Sanavio, M. Glottenberg, L. Casalis, C. M. Niemeyer, G. Scoles, *Nano Lett.* **2009**, *9*, 2614.
- [62] M. Castronovo, S. Radovic, C. Grunwald, L. Casalis, M. Morgante, G. Scoles, *Nano Lett.* **2008**, *8*, 4140.
- [63] C. Staii, D. W. Wood, G. Scoles, *Nano Lett.* **2008**, *8*, 2503.

- [64] S. Xu, N. A. Amro, G. Y. Liu, *Appl. Surf. Sci.* **2001**, 175–176, 649.
- [65] D. Scaini, M. Castronovo, L. Casalis, G. Scoles, *ACS Nano* **2008**, 2, 507.
- [66] L. G. Rosa, J. Liang, *J. Phys.: Condens. Matter* **2009**, 21, 483001.
- [67] J. te Riet, T. Smit, J. W. Gerritsen, A. Cambi, J. A. A. W. Elemans, C. G. Figdor, S. Speller, *Langmuir* **2010**, 26, 6357.
- [68] M. Castronovo, F. Bano, S. Raugei, D. Scaini, M. Dell'Angela, R. Hudej, L. Casalis, G. Scoles, *J. Am. Chem. Soc.* **2007**, 129, 2636.
- [69] J. Liang, M. Castronovo, G. Scoles, *J. Am. Chem. Soc.* **2012**, 134, 39.
- [70] G. E. Yakubov, J. Mccoll, J. H. H. Bongaerts, J. J. Ramsden, *Society* **2009**, 25, 2313.
- [71] MacL. Akova, G. E. Yakubov, M. A. Plunkett, J. R. Stokes, *Tribol. Int.* **2011**, 44, 956.
- [72] O. Torres, E. Andablo-Reyes, B. S. Murray, A. Sarkar, *ACS Appl. Mater. Interfaces* **2018**, 10, 26893.
- [73] N. Vassilakos, T. Arnebrant, P.-O. Glantz, *Eur. J. Oral Sci.* **1992**, 100, 346.
- [74] A. Sarkar, F. Kanti, A. Gulotta, B. S. Murray, S. Zhang, *Langmuir* **2017**, 33, 14699.
- [75] C. Myant, H. A. Spikes, J. R. Stokes, *Tribol. Int.* **2010**, 43, 55.
- [76] E. M. Krop, M. M. Hetherington, M. Holmes, S. Miquel, A. Sarkar, *Food Hydrocolloids* **2019**, 88, 101.
- [77] L. Laguna, G. Farrell, M. Bryant, A. Morina, A. Sarkar, *Food Funct.* **2017**, 8, 563.
- [78] E. Dickinson, V. J. Pinfield, D. S. Horne, F. A. M. Leermakers, *J. Chem. Soc., Faraday Trans.* **1997**, 93, 1785.
- [79] R. Ettelaie, A. Akinshina, *Food Hydrocolloids* **2014**, 42, 106.
- [80] R. Ettelaie, A. Akinshina, E. Dickinson, *Faraday Discuss.* **2008**, 139, 161.
- [81] R. Ettelaie, A. Akinshina, S. Maurer, *Soft Matter* **2012**, 8, 7582.
- [82] A. Akinshina, R. Ettelaie, E. Dickinson, G. Smyth, *Biomacromolecules* **2008**, 9, 3188.
- [83] F. A. M. Leermakers, P. J. Atkinson, E. Dickinson, D. S. Horne, *J. Colloid Interface Sci.* **1996**, 178, 681.
- [84] O. A. Evers, J. M. H. M. Scheutjens, G. J. Fleer, *Macromolecules* **1991**, 24, 5558.
- [85] V. Dinu, R. B. Gillis, T. Mac Calman, M. Lim, G. G. Adams, S. E. Harding, I. D. Fisk, *Food Biophys.* **2019**, 14, 278.